Oxytocin neurons signal state-dependent transitions to thermogenesis and behavioral arousal in social and non-social settings

Morgane Vandendoren[1#], Joseph F. Rogers[1#], Jason G. Landen[1], Samantha Killmer[1], Baizar Alimiri[1], Celeste Pohlman[1], Glenn J. Tattersall[2], Nicole L. Bedford[1], Adam C. Nelson[1*]

1) Department of Zoology and Physiology, University of Wyoming, Laramie, WY, USA.
2) Department of Biological Sciences, Brock University, St Catharines, Ontario, Canada

[#] These authors contributed equally

* Corresponding author: Adam C Nelson, anelso74@uwyo.edu

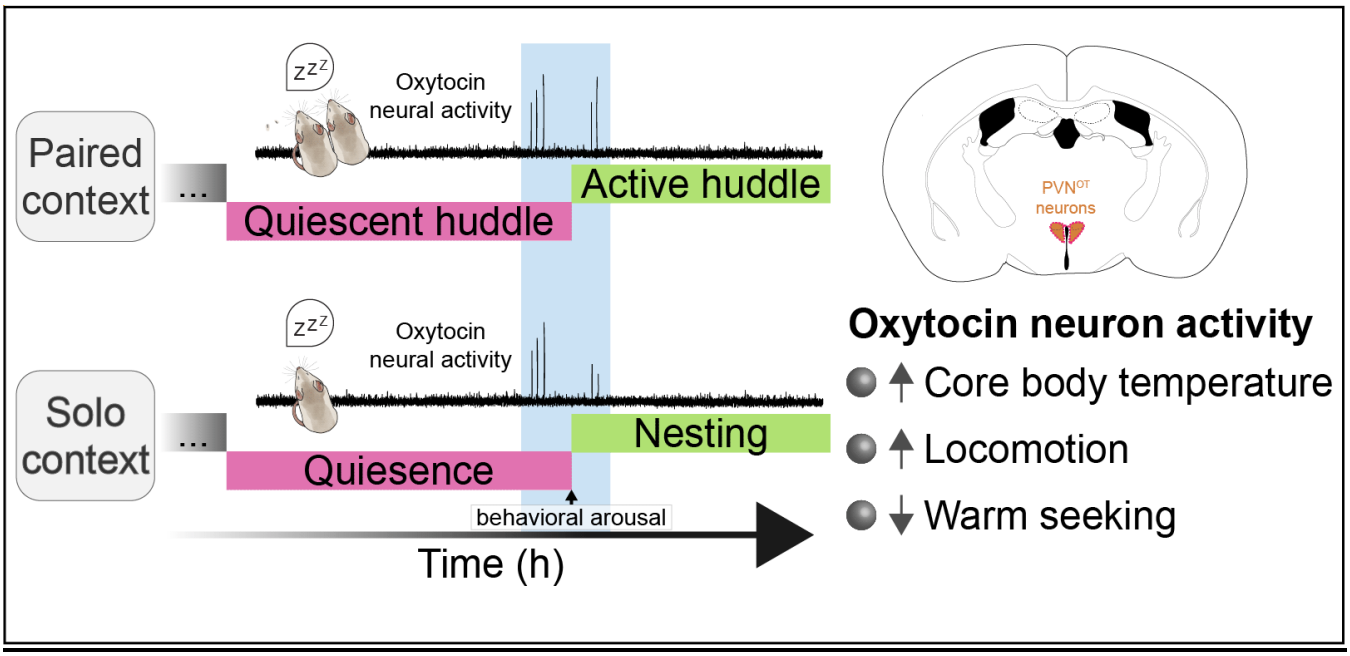

Graphical Abstract

Abstract
Mammalian thermoregulatory behaviors such as thermal comfort seeking, physical activity, nesting, and huddling operate alongside autonomic responses such as brown fat thermogenesis and peripheral vasodilation to defend core body temperature (Tb)[1–4]. The defended Tb is not held constant, but alternates across active/rest and behavioral cycles[5–9]. Although the thermoregulatory behaviors facilitating these alternations are controlled by the brain, the underlying neural populations are poorly understood. The oxytocin system has been proposed to contribute to behavioral thermoregulation[10,11], yet evidence for how activity within oxytocin neurons relates to such pathways is lacking. Here, we identify neuronal dynamics underlying behavioral thermoregulation in mice. We show that the paraventricular hypothalamus (PVN) and PVN oxytocin (PVN^{OT}) neurons are selectively activated during two thermoregulatory states: active and quiescent huddling. Next, activation and inhibition of PVN^{OT} neurons reveals effects on Tb, peripheral vasodilation, and warm seeking, establishing a role in thermoeffector pathways. We then demonstrate that *in vivo* PVN^{OT} calcium activity tracks the patterning of thermoregulatory behaviors. Across social contexts, PVN^{OT} peaks occur during low Tb (~36.0°C) and during transitions towards physical activity and thermogenesis. In the solo context, PVN^{OT} peaks predict the offset of quiescence and onset of post-quiescence nesting. In the paired context, PVN^{OT} peaks predict the offset of quiescent huddling and onset of post-quiescent active huddling. Our study provides evidence for a role of PVN^{OT} neurons during the offset of rest and the onset of behavioral arousal and thermogenesis and provides a foundation for understanding the coordination between thermal homeostasis and animal behavior.

Results and Discussion
Maintaining a relatively constant core body temperature (Tb) is a vital homeostatic need. In mammals, excessive deviations (e.g., >2°C) from a mean Tb of approximately 37°C can lead to lead to dangerous physiological challenges [12]. However, Tb naturally fluctuates within a narrow range (e.g., 0.5 to 1°C) across daily life and behavioral states in a bimodal or multimodal fashion [5,6,13]. Accumulating evidence suggests these fluctuations are not a passive consequence of animal physiology, but instead a regulated, brain-initiated defense of multiple “balance-points” [8] adapted for particular behavioral and metabolic states [2,5,7]. Such balance-points alternate across the diurnal cycle and stages of sleep, as well as during fever, hibernation, and food deprivation [6,8,9,14–18]. For example, the transition from the “rest” to “active” balance-point is accompanied by modulation of autonomic and behavioral thermoeffector pathways (i.e., processes regulating heat loss and production) to increase Tb [5,7,9]. Yet, a gap in our understanding is that the neural populations underlying such transitions are poorly understood.

Autonomic thermoregulatory information flows from afferent thermoreceptor neurons to the preoptic area of the hypothalamus (POA), to the dorsomedial hypothalamus (DMH), and on to sympathetic efferent neurons of the rostral medullary raphe (rMR) [2,19]. The POA is the primary integration site of thermal inputs to drive autonomic responses such as peripheral vasodilation and heat production from muscle and brown adipose tissue (BAT). The neuromodulators, receptors, and projections that respond to thermal challenge are increasingly understood [20–23]. In contrast, our understanding of circuits underlying behavioral thermoregulation is limited [3]. Notably, the POA is not required for most forms of behavioral thermoregulation [8,23,24]. Although recent studies have made progress in identifying brain regions underlying some pathways, including neural populations in the DMH, median preoptic nucleus, lateral hypothalamus, and central amygdala [3,23,25,26], much is still unknown about how animals behaviorally thermoregulate.

Mice are a model organism for studies of energy regulation and animal behavior alike. Because laboratory mice are housed below their thermoneutral zone (i.e., the ambient temperature where metabolic rate is at a minimum) [27] and exert around one-third of their energy budget on cold-induced thermogenesis [17], understanding the circuits underlying naturalistic thermoregulation is informative. Mouse thermoregulatory behaviors include thermal comfort seeking, nesting, physical activity (locomotion), and huddling [7,27–29]. Mice exhibit two huddling substates: active huddling (i.e., maintaining physical contact while displaying movement) and quiescent huddling (i.e., maintaining physical contact while motionless). Both substates are associated with, on average, a low Tb and an energy saving state [28]. However, active-huddling facilitates bidirectional Tb changes: Tb decreases before, and increases after, bouts of quiescent huddling [28]. Huddling also serves social functions. For example, mice prefer a cold environment where they are allowed to huddle over isolation in a thermoneutral environment [30]. Understanding the circuits underlying huddling could provide an inroad to understanding brain-body links between Tb and social/affective states [31–34]. However, the location, identity, and function of huddling-associated neurons is not known. Here, we set out to identify brain regions and cell types associated with daily patterns of behavioral thermoregulation in mice.

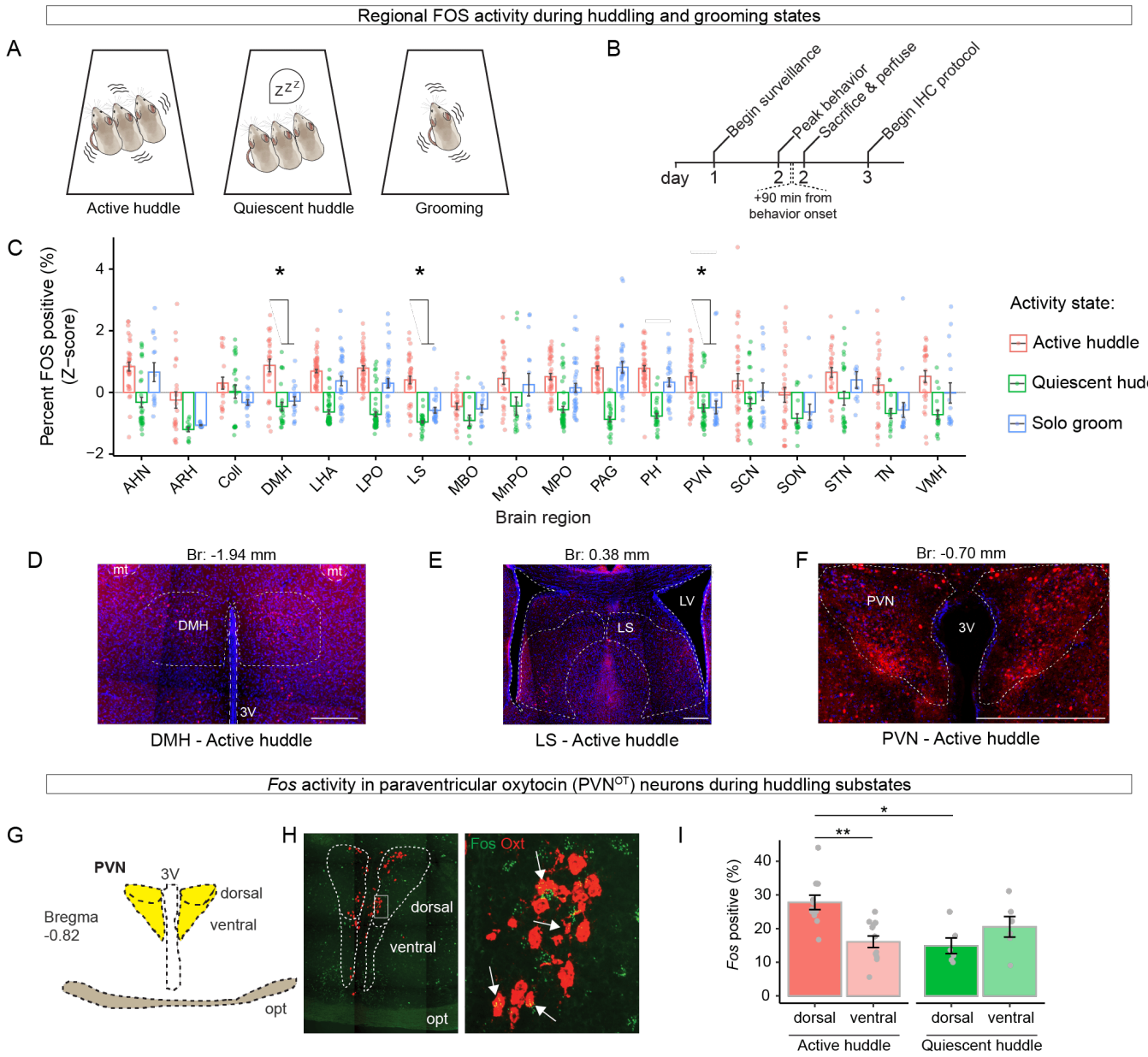

Figure 1. The PVN and PVN^{OT} neurons are FOS activated during huddling substates.
(A - B) Experimental design to identify state-specific activity in 18 brain regions. Behavioral states **(A)**. Experimental timeline **(B)**.
(C) Quantification of percent FOS - DAPI colocalized cells across brain regions for each behavior. Regional FOS percentages are z-scored on a per experiment basis. N = 15 mice/1530 ROIs. Each datapoint is an ROI. Asterisks denote regions in which active huddle FOS activity is greater than both quiescent huddle and solo groom. P-values adjusted for multiple comparisons using the Holm method.
(D - F) Representative histology images showing active huddling associated FOS expression in the DMH **(D)**, LS **(E)**, and PVN **(F)**. 3V: third ventricle; mt: mammillothalamic tract; LV: lateral ventricle. Scale bar equals 500 µm.
(G) Schematic of the PVN. Opt: optic tract.
(H) Representative histology images showing mRNA expression of *Fos* and *Oxt* in the PVN.
(I) Quantification of percent *Fos*:DAPI colocalized cells in dorsal and ventral subregions of the PVN during active huddling and quiescent huddling (N = 8 mice). Each datapoint is an ROI.
C: linear model with Tukey's post-hoc tests. **I:** linear mixed effect model. Data are mean ±SEM. P < 0.05 *, P < 0.01 **, P < 0.001 ***. Full statistical analysis in Table S1.

PVN^{OT} neural activity is associated with huddling substates.

We sought to identify huddling-associated brain regions in adult female groups, which we previously found show stronger huddling-associated Tb changes than male groups [28]. Using a home-cage surveillance system that eliminates direct human-animal interaction [28] in conjunction with FOS immunohistochemistry (IHC), we examined patterns of

activity in 18 brain regions. We focused on regions associated with thermoregulation, social behavior, and identified to be FOS activated during huddling substates in preliminary studies (Fig. 1A-B). We examined animals engaged in active huddling, quiescent huddling and, as a control for physical touch in the absence of social contact, solo-housed animals engaged in self-grooming. For IHC, we scored cellular FOS activity after the animals had been engaged in state-specific behavior (i.e., active huddle, quiescent huddle, solo-groom) for at least 15 minutes.

We first investigated FOS expression in brain regions associated with purposeful huddling (i.e., active huddling). We identified three active huddling associated regions: the dorsal medial hypothalamus (DMH), the rostral lateral septum (LS), and the paraventricular nucleus of the hypothalamus (PVN) (Fig. 1C-F and S1A-C). The DMH and the PH are areas associated with energy regulation, thermoregulation, and inputs to the rMR [2,35,36]. The LS is associated with a variety of functions, from motivation to fear responses [37,38], and is notably associated with the control of social behavior [39]. These results suggest active huddling recruits brain regions with known roles in thermoeffector and social interaction pathways.

Hypothalamic oxytocin (OT) neurons are a candidate population linking thermoregulation with affective and social behavior [10,34,40,41]. Notably, the PVN is one of the two primary locations of OT-producing neurons [36]. Oxytocin neurons have a well-established role in the modulation of social behavior, particularly the salience of social stimuli [42,43], while a mostly separate literature implicates oxytocin in thermosensation [10,40], thermoregulation [44–46], and energy expenditure [47]. Intriguingly, OT-mutant rat pups display deficits in both warm-seeking and huddling behavior [41]. However, how hypothalamic oxytocin neurons encode information relevant to thermoregulatory states is not known.

We asked whether paraventricular oxytocin neurons (i.e., PVN^{OT}) neurons were activated during active and quiescent huddling. Using single-molecule fluorescence *in situ* hybridization (smFISH), we quantified *Fos*-positive PVN^{OT} neurons in the dorsal and ventral portions of the PVN, which have unique cyto-architectures and projection patterns [48] (Fig. 1G-I). PVN^{OT} neurons were *Fos*-positive during both active huddling and quiescent huddling. During active huddling, the dorsal population was more *Fos*-positive than the ventral population, and this dorsal population displayed greater *Fos* activity during active compared to quiescent huddling (Fig. 1I). These results suggest the PVN is a huddling-associated brain region and that PVN^{OT} neurons are differentially activated during huddling substates. PVN^{OT} neurons are therefore a candidate population underlying behavioral thermoregulation.

PVN^{OT} excitation increases Tb, decreases warm seeking, and increases peripheral vasodilation.
Paraventricular hypothalamic OT neurons are involved in thermogenesis in rats [44], but the function of PVN^{OT} neurons in mouse thermoeffector pathways has not been explored. We therefore sought to determine whether manipulation of PVN^{OT} neurons during thermal challenge affected a set of thermogenic responses: core Tb; surface temperatures overlying intrascapular BAT (iBAT), trunk, and tail; and warm seeking during cold exposure (Fig. 2A-B). We used excitatory (AAV-hSyn-DIO-hM3D(Gq)-mCherry) and inhibitory (AAV-hSyn-DIO-hM4D(Gi)-mCherry) DREADD AAVs [49] that have been validated for Cre-dependent transfection of OT-positive neurons [50,51] (Fig. S1D-E). AAVs were injected into the PVN of OT-Cre mice (Fig 2C-D). These injections covered the rostral to causal axis of the PVN. Each animal was investigated in a longitudinal study involving three 15-minute conditions in a temperature-controlled chamber: cold exposure (15°C); cold exposure with access to a warm pedestal (22°C) for the last five minutes; and warm exposure (32°C, a temperature near mouse thermoneutrality [18,27,52,53]). Core Tb was measured with implanted temperature loggers; surface temperature of iBAT, trunk, and tail were measured with thermography; and warm seeking was measured as time spent on the pedestal (22°C) (Methods).

Deschloroclozapine (DCZ) is a potent DREADD ligand [54] with advantages over the ligand clozapine-*N*-oxide (CNO) because CNO can be reverse-metabolized to clozapine to exert clozapine-like behavioral effects [55]. Clozapine can also reduce Tb and increase cutaneous vasodilation [56–58]. Conversely, DCZ has few known side effects [59]. We administered DCZ systemically through intraperitoneal injections (0.1 mg/kg). In control experiments, we found DCZ alone had no discernable effect on Tb, warm seeking, and peripheral vasodilation (Fig. S2A-G). Unexpectedly, however, DCZ affected physical activity (Fig. 2E-G). In experiments conducted at 15°C, animals receiving vehicle injections generally maintained locomotion throughout the 15-minute trial, while animals receiving DCZ injections displayed moments of inactivity (Fig. 2E). Moreover, most animals displayed reduced activity when receiving DCZ compared to vehicle (Fig. 2G). To account for this off-target drug effect, we used statistical approaches that partition variance in Tb and warm-seeking that is attributable to drug (DCZ *vs*. vehicle), physical activity, and their interaction (Methods).

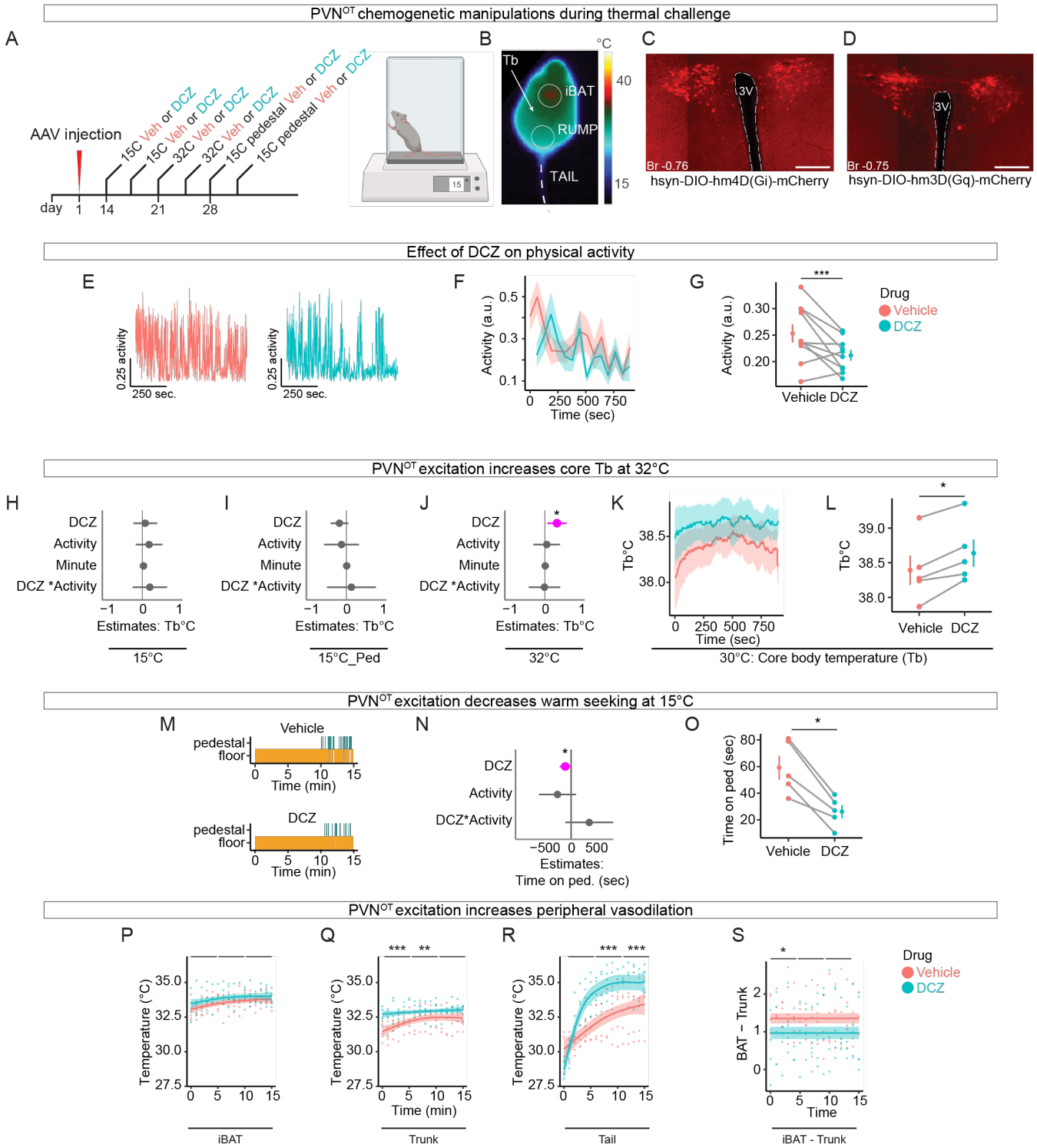

Figure 2. Chemogenetic activation of PVN^{OT} cells increases core body temperature and peripheral vasodilation, and decreases suppresses warm seeking.

(A - D) Scheme of DREADD experiments and hot/cold plate arena used for floor temperature control **(A)**. Features of the thermal profile; areas quantified from thermography (BAT, trunk, and tail) and core body temperature (Tb) **(B)**. Histology showing inhibitory and excitatory DREADDs in the PVN of OT-Cre mice **(C-D)**.

(E - G) Effects of DCZ on locomotion. Activity traces from one mouse during vehicle (left) and DCZ (right) injections **(E)**. Mean activity levels according to injection type **(F)**. Per-individual mean activity in the 15C and 15C_Pedestal experiments according to injection **(G)**.

(H - L) PVN^{OT} excitation increases core Tb. Forest plots show effect of PVN^{OT} excitation on Tb, activity, time, and activity*time interaction **(H-J)**. No effect of PVN^{OT} excitation on Tb in the 15°C **(H)** and 15°C_Pedestal **(I)** experiments. PVN^{OT} excitation causes increase Tb at 32°C **(J)**. Mean Tb over time according to drug (DCZ or vehicle) **(K)**. Per-individual mean Tb according to drug **(L)**.

(M – O) PVN^{OT} excitation decreases warm seeking. Representative ethogram showing time on pedestal of an animal during vehicle (top) and DCZ (bottom) injections **(M)**. Forest plots show effect of excitation on time on pedestal, activity, and their interaction **(N)**. Per-individual time on pedestal according to drug (DCZ or vehicle) **(O)**.

Fig. 2 cont'd. (P - S) PVN^{OT} excitation increases peripheral vasodilation. Effect of excitation on the surface temperature of iBAT **(P)**, trunk **(Q)**, tail **(R)**, and the iBAT-trunk difference **(S)** over time. Solid lines show mean temperature and shaded areas standard error. Analyses were divided into three five-minute intervals (top). P-values are adjusted for multiple corrections using the Holm method.
G: linear mixed model. **H,I,J,L,N,O,P,Q,R,S**: autoregressive mixed model. DCZ control N = 5 mice. 15°C, 15°C_pedestal, 32°C N = 5 mice. **P,Q,R,S** show predicted values of a general additive model. **H, I, J, N** show mean and confidence intervals. All else show mean ±SEM. P < 0.05 *, P < 0.01 **, P < 0.001 ***. Full statistical analysis in Table S1.

We then examined the effect of chemogenetic activation of PVN^{OT} neurons on the thermal profile of female mice (Fig. 2H-L and Fig. S2H-L). As before, presence of DCZ was associated with reduced activity (Fig. S2H). PVN^{OT} activation did not affect Tb in the 15°C experiments (Fig. 2H-I). In contrast, PVN^{OT} activation at 32°C led to a significant increase in Tb (Fig. 2J-L). Using a linear mixed model that accounts for temporal autocorrelation in Tb, we found that PVN^{OT} activation increased Tb by an estimated 0.34°C ± 0.13 °C while controlling for other factors (Fig. 2J). PVN^{OT} activation also resulted in less time-spent on the warm pedestal (Fig. 2M-O), leading to an estimated 115.4 ± 39.6 fewer seconds compared to vehicle injection while controlling for other factors (Fig. 2N). PVN^{OT} activation at 32°C also resulted in an increase in the surface temperature (i.e., vasodilation) of the trunk and tail, but not iBAT temperature (Fig. 2P-S). Similar vasomotor effects were observed in the 15°C experiments (Fig. S2M-P). These results suggest that activation of PVN^{OT} neurons can drive an increase in Tb and a decrease in warm seeking behavior, as well as an increase in peripheral vasodilation of the trunk and tail. Notably, this profile is distinct from the stress response, which is associated with increased Tb due iBAT thermogenesis and reduced peripheral vasodilation [1].

Next, we examined the effect of PVN^{OT} chemogenetic inhibition. We found no effects of DCZ-mediated inhibition on Tb (Fig. S2Q-V) or warm seeking (Fig. S2W-X). However, DCZ-mediated inhibition did affect peripheral vasodilation in a pattern markedly similar to that observed in the excitatory experiments: PVN^{OT} activation at 32°C resulted in increased vasodilation of the trunk and tail throughout the trial, but iBAT temperature was unaffected (Fig. S2Y-Z). Because both excitation and inhibition of PVN^{OT} cells results in vasodilation at 32°C—an effect not due to DCZ administration (Fig. S2E-G)—these results could suggest the presence of PVN^{OT} sub-populations with distinct microcircuit motifs (e.g., feedforward/feedback pathways of excitation and inhibition) relevant to thermoregulation, or neuronal homeostatic or plasticity responses to sustained chemogenetic inhibition [60]. Taken together, these experiments suggest that PVN^{OT} neurons are capable of modulating thermoeffector pathways relevant to thermoregulation.

PVN^{OT} calcium peaks track quiescence, nesting, and huddling states in solo and paired animals.
The sufficiency of PVN^{OT} neurons to modulate the thermal profile suggests they may encode important aspects of thermoeffector pathways. Behaviorally, mice modulate body temperature through physical activity, nesting, and huddling [7,27–29]. We asked how calcium activity in PVN^{OT} neurons was associated with real-time behavior under different social and thermal conditions. We used AAVs encoding the calcium indicator GCaMP (pGP-AAV9-syn-FLEX-jGCaMP8s-WPRE; pAAV.Syn.GCaMP6f.WPRE.SV40) [61] and fiber photometry using an optical fiber implanted above the PVN (Fig. 3A-D). GCaMP AAVs have been validated to transfect OT neurons in OT-Cre mice [62–64]. In a longitudinal study accounting for individual variance in behavior and physiology, we examined the state-specificity of PVN^{OT} calcium responses in solo and paired conditions at three floor temperatures: a cold temperature (15°C), room temperature (23°C), and a temperature near the lower critical temperature (i.e., the point of transition between energy-requiring and energy-neutral thermoregulatory mechanisms; 29°C [18,27,53]). Photometric recordings were conducted during the light/rest phase, when thermoregulatory behaviors are more common [28]. We observed pulsatile calcium peaks similar to those previously reported in female mice [63] (Fig. 3D). Analyses focused only on peaks that were at least six standard deviations above the baseline (Methods).

We first examined the effect of social context on calcium peak amplitude and frequency across the three floor temperatures. There was no total effect of social context on peak amplitude or frequency (Fig. S3B-C). However, PVN^{OT} peaks were associated with distinct behaviors in a social-context dependent manner. In the solo context, peak amplitude and frequency were associated with nesting and quiescence (Fig. 3E-G). In the paired context, calcium peaks were associated with active and quiescent huddling (Supplementary Video 1), and to a lesser extent, nesting (Fig. 3H-J). We then examined the behavioral associations of PVN^{OT} peaks within each floor temperature. Strikingly, the behavior-state associations with calcium peaks were largely preserved across all three conditions (Fig. S3F-I). Linear mixed model analysis of calcium peaks revealed main effects of quiescence and nesting in the solo context (Fig. S3F,H), and main effects of active huddling, quiescent huddling, and nesting in the paired context (Fig. S3G,I).

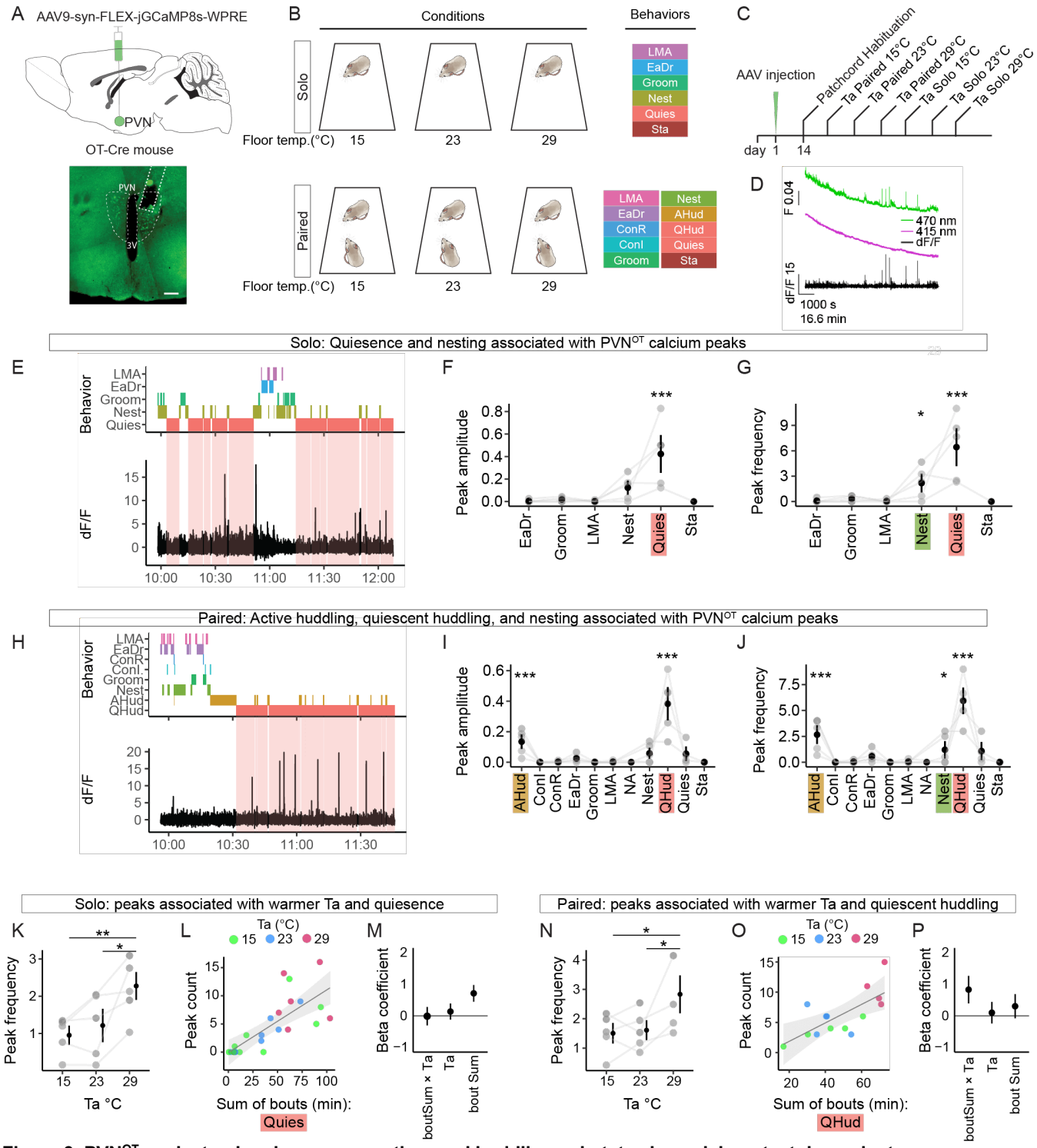

Figure 3. PVN^OT peaks track quiescence, nesting, and huddling substates in social-context dependent manner.
(A - C) Fiber photometric recordings of PVN^OT cells in different social contexts and floor temperature conditions. Scheme of GCaMP AAV injections (top) and histology showing GCaMP-positive neurons in the PVN optic fiber placement (bottom) Scale bar 200 µm. **(A)**. Floor temperature and social context conditions, and behaviors analyzed **(B)**. Scheme of the timeline. Order of the social and floor temperature conditions was pseudo-randomized **(C)**.
(D) Example traces of calcium-dependent (470 nm) and calcium-independent (415 nm) channels, and the post-processed dF/F trace (bottom), from a two-hour recording.
(E - F) Behaviors associated with PVN^OT peaks in solo condition. Example ethogram aligned to photometric recording. Soft red shaded areas align with the quiescent state **(E)**. PVN^OT peak amplitude **(F)** and frequency **(G)** according to behavioral state across solo trials.
(H - J) Behaviors associated with PVN^OT peaks in paired condition. Example ethogram aligned to photometric recording. Soft red shaded areas align with quiescent huddling **(H)**. PVN^OT peak amplitude **(I)** and frequency **(J)** according to behavioral state across paired trials.

Fig. 3 cont'd. (K – M) Effect of floor temperature and quiescence on PVN^{OT} peaks in solo animals. Peak frequency according to floor temperature (Ta) **(K)**. Peak count according to total duration of quiescent bouts **(L)**. Beta coefficients from a model of the effect of floor temperature, total duration of bouts (boutSum), and the Ta*boutSum interaction on peak count **(M)**.
(N – P) Effect of floor temperature and quiescence huddling on PVN^{OT} peaks in paired animals. PVN^{OT} peak frequency according to floor temperature **(N)**. Peak count according to total duration of quiescent bouts **(O)**. Beta coefficients from a model of the effect of floor temperature, total duration of bouts (boutSum), and the Ta*boutSum interaction on peak count **(P)**.
F,G,I,J,K,L,M,N,O,P: linear mixed model. N = 5 mice/30 recordings. **M** and **P** show means plus confidence interval; all else shows mean ±SEM. P < 0.05 *, P < 0.01 **, P < 0.001 ***. Full statistical analysis in Table S1.

Next, we analyzed the effect of floor temperature on peak frequency across the two social contexts (Fig. 3K-P). Peaks were more frequent at the warmer temperature (29°C) for both solo (Fig. 3K) and paired (Fig. 3N) animals. In mice, sleep is more common at warmer ambient temperatures [9]. To disambiguate whether PVN^{OT} peaks display warm sensitivity *per se*, we performed a regression analysis relating the number of peaks to the floor temperature as well as the duration of bouts of rest (i.e., quiescence for solo mice and quiescent huddling for paired mice) (Fig. 3F-G and I-J). In both the solo and paired condition, calcium peak counts were strongly related to bout duration of quiescence and quiescent huddling, respectively (Fig. 3L,O). In this analysis, bouts of quiescence and quiescent huddling appeared longer at 29°C (Fig. 3L,O, red dots). We therefore examined the contribution of bout length, floor temperature, and their interaction to peak counts. In the solo context, increased peak counts at 29°C could be explained by longer quiescence bout lengths (Fig. 3M). In the paired context, increased peak counts at 29°C could be explained by the interaction between bout length and floor temperature (Fig. 3P). Taken together, these results suggest PVN^{OT} peaks track quiescence, quiescent huddling, nesting, and active huddling in a social-context dependent manner, and are largely unaffected by the ambient conditions tested. In subsequent analyses, we therefore pooled data from the three floor temperatures.

PVN^{OT} neurons predict social-context dependent transitions towards behavioral arousal and thermogenesis

Our analysis showed that PVN^{OT} peaks track two rest states (quiescence and quiescent huddling), and two active states (i.e., nesting and active huddling). Notably, each of these states are in part thermoregulatory and are naturally organized into alternating sequences across the daily cycle [9,28,30,65–68]. To address how PVN^{OT} dynamics aligned with these sequences, we quantified peaks relative to the onset and offset of behavior bouts in the homecage, as well as to changes in locomotion and core body temperature (Fig. 4A).

We first examined locomotion before and after PVN^{OT} calcium peaks in the homecage. In both solo and paired conditions, locomotion increased following PVN^{OT} peaks. This increase began at the approximate time of the peak and persisted through the subsequent 200 seconds (Fig. 4B-E). We next examined the density of peaks with respect to the onset and offset of the two resting states: quiescence and quiescent huddling. For both behaviors, there was a higher density of peaks in the minutes prior to bout offset compared to onset (Fig. S4A-F). Moreover, there was a positive relationship between bout length and the number of peaks, indicating that longer bouts are more likely to have peaks (Fig. S4C,F). To better understand the relationship between PVN^{OT} dynamics and bouts of quiescence and quiescence huddling, we modelled the per-second probability of observing a peak relative to bout onset and offset using logistic regression (Fig. 4F-O, Methods). For bouts of quiescence, peak probability was approximately 3.2% near the time of onset and 15.0% near the time of offset (Fig. 4F-G). For bouts of quiescent huddling, peak probability was approximately 2.5% near the onset and around 20.7% near the time of offset (Fig. H-I). Thus, PVN^{OT} peaks predict the offset of quiescence and quiescent huddling bouts and an increase in locomotion, a correlate of behavioral arousal [69].

We next examined PVN^{OT} peak density and probability during the onset and offset of the two active states: nesting and active huddling (Fig. 4F-O, and S4G-L). In contrast to the two resting states, peak density appeared higher in the minutes following onset of both types of bouts (Fig. S4G,H,J,K). Moreover, there was a weak relationship between peak count and bout length for both nesting and active huddling, indicating that longer bouts are not more likely to have peaks (Fig. S4I,L). Logistic regression analysis of nesting bouts showed that PVN^{OT} peak probability was approximately 7.3% near the time of onset and 2.6% near the time of offset (Fig. 4J-K). For active huddling bouts, peak probability was approximately 12.5% near the time of onset and 2.6% near the time of offset (Fig. 4M-N). Thus, PVN^{OT} peaks are more likely to predict bout onset of nesting and active huddling. Notably, within the paired condition, there was a higher peak probability for active huddling comparted to nesting (Poisson regression, nesting vs. active huddling peaks counts, P < 0.001).

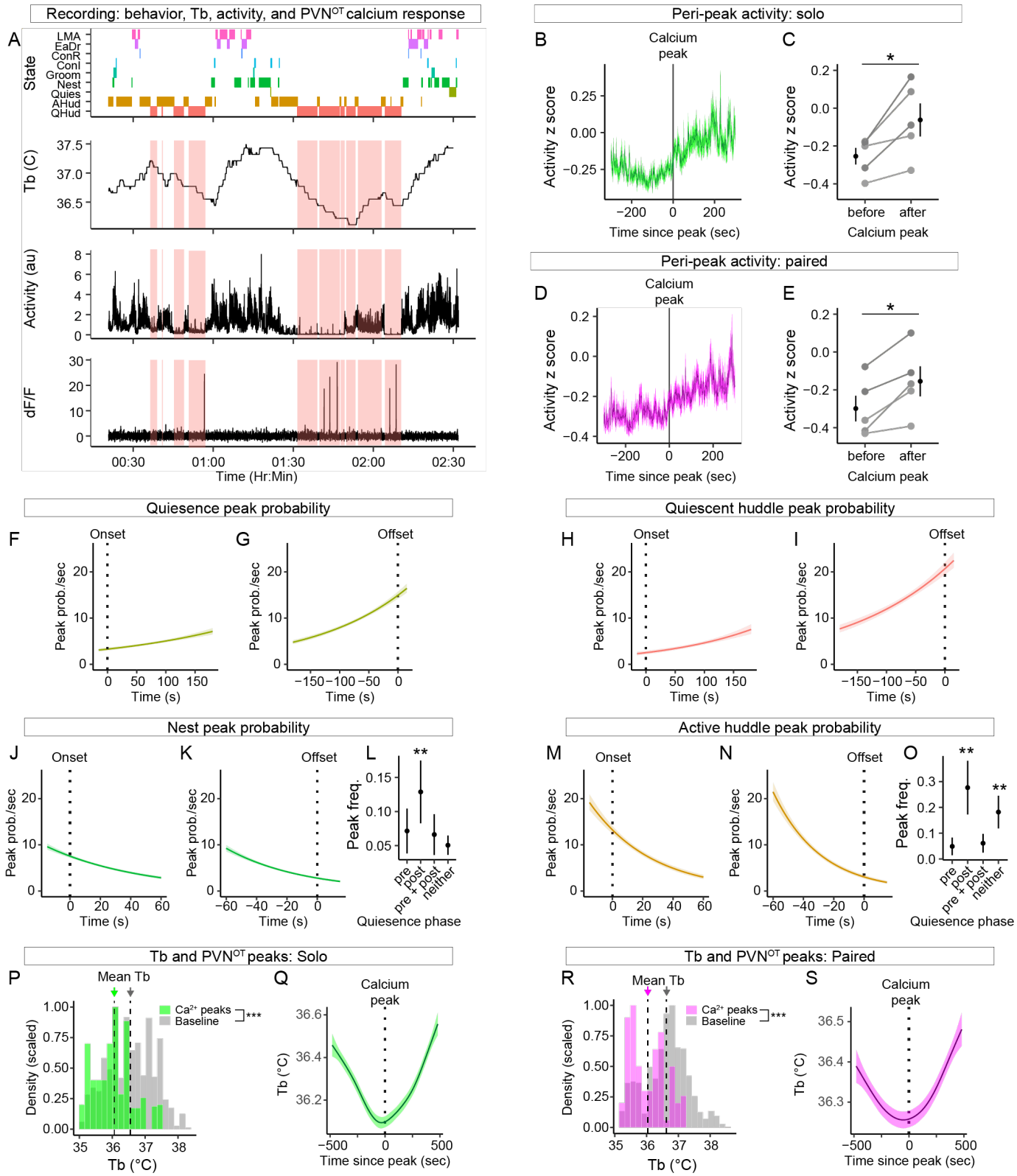

Figure 4. PVN^{OT} peaks predict transitions to behavioral arousal and thermogenesis.
(A) Alignment of behavioral state, body temperature, physical activity, and dF/F from an experiment in the paired context.
(B-E) PVN^{OT} peaks and physical activity. Peri-event time histogram of activity before and after PVN^{OT} peaks in solo mice **(B)**. Per-individual means before and after PVN^{OT} peaks in solo mice **(C)**. Peri-event time histogram of activity before and after peaks in paired mice **(D)**. Per-individual means before and after peaks in paired mice **(E)**.

Fig. 4 cont'd. **(F - O)** PVN^{OT} dynamics during onset and offset of behavior bouts. Peak probability during quiescence onset **(F)**. Peak probability during quiescence offset **(G)**. Peak probability during quiescent huddle onset **(H)**. Peak probability during quiescent huddle offset **(I)**. Peak probability during nesting onset **(J)**. Peak probability during nesting offset **(K)**. Nesting-associated peak frequency according to the phase of quiescence. "Neither" refers to bouts that did not adjoin bouts of quiescence **(L)**. Peak probability during active huddling onset **(M)**. Peak probability during active huddling offset **(N)**. Active huddling-associated peak frequency according to the phase of quiescence **(O)**.
(P-S) PVN^{OT} dynamics and core body temperature. Histogram of body temperature during minutes containing a calcium peak (green) vs. baseline (grey) data in solo animals **(P)**. Peri-event time histogram of body temperature before and after PVN^{OT} peaks in solo animals **(Q)**. Histogram of body temperature during minutes containing a calcium peak (green) vs. baseline (grey) data in paired animals **(R)**. Peri-event time histogram of body temperature before and after PVN^{OT} peaks in paired animals **(S)**.
C,E,L,O,P,R: linear mixed model. **F,G,H,I,J,K,M,N**: logistic regression. N = 5 mice/30 recordings, except for P-S, N = 4 mice/14 recordings. **Q** and **S** show predicted values of a general additive model; all data shows mean ±SEM. $P < 0.05$ *, $P < 0.01$ **, $P < 0.001$ ***. Full statistical analysis in Table S1.

Nesting and active huddling often occur immediately before or after (or in between) bouts of quiescence (i.e., the peri-quiescent phase) [28,30,66,68]. We next examined the phase of quiescence for peaks associated with nesting and active huddling. PVN^{OT} peaks were more likely to occur during the post-quiescence phase for both nesting (Fig. 4L) and active huddling (Fig. 4O). Notably, although nesting and active huddling are commonly expressed during the pre-quiescent phase (or outside of the quiescent phase), these two behaviors are relatively rare during the post-quiescent phase (Fig. S4M-N). Thus, although nesting and active huddling are less likely to occur post quiescence, PVN^{OT} peaks are more likely during that phase. This suggests that PVN^{OT} neurons distinguish nesting and active huddling in the post-quiescent phase from the pre-quiescent phase. Together, these results suggest that PVN^{OT} activity dynamics predict within approximately 100 seconds the offset of two rest states (quiescence and quiescent huddling) and predict within around 20 seconds the onset of two active states (nesting and active huddling) during the post-quiescence phase.

PVN^{OT} peaks occur during a low Tb (~36.0°C) and prior to body warming.
In rodents, transitions from rest to arousal are proposed to result in part from an ultradian (i.e., occurring on cycles < 24 hr), brain-driven switch of the defended body temperature from a rest balance-point to an awake balance-point [5,7]. Because PVN^{OT} peaks aligned with transitions from resting to active states, we next examined individual core body temperature dynamics before, during, and after PVN^{OT} peaks (Fig. 4P-S). In both the solo and paired conditions, PVN^{OT} peaks occurred at a Tb significantly lower than baseline (solo: baseline-Tb 36.55°C, peri-peak-Tb 36.06°C; paired: baseline-Tb 36.61°C, peri-peak-Tb 36.04°C) (Fig. 4P,R). Moreover, PVN^{OT} peaks aligned with the low point of a U-shaped body temperature profile: on average, Tb decreased before, and increased after, the time of the calcium peak in both solo and paired conditions (Fig. 4Q,S). Together, these results suggest that PVN^{OT} peaks signal occur during a low body temperature and predict a forthcoming increase in Tb.

By what pathways could PVN^{OT} neurons promote transitions towards thermogenesis and locomotion? rMR efferent neurons regulate non-shivering thermogenesis, cutaneous vasoconstriction, and heart rate [2], and the surrounding gigantocellular reticular nucleus (GiA) regulates locomotion and movement [70,71]. Moreover, in rats PVN^{OT} to rMR projections (PVN^{OT}→rMR) stimulate thermogenesis and cardiovascular responses in an oxytocin receptor (OXTR) dependent fashion [44]. To investigate possible PVN^{OT}→rMR cell types in mice, we used tracing tools to disambiguate magno- vs. parvocellular PVN^{OT} projections [72] (Fig. S4O-P). The majority of PVN^{OT}→rMR projections were non-magnocellular cells located in the caudal and lateral PVN, suggesting they are parvocellular (i.e., $PVN^{OT(parvo)}$) (Fig. S4Q), consistent with previous studies [44,72,73]. In addition, we observed OXTR-positive neurons in the rMR and GiA (i.e., rMR^{OXTR}) using smFISH (Fig. S4R). Thus, $PVN^{OT(Parvo)}$→rMR^{OXTR} neurons are a candidate pathway underlying transitions towards arousal and thermogenesis in mice.

Conclusions
This study expands our understanding of *in vivo* PVN^{OT} responses [62–64,74,75] by demonstrating how they align with patterns of innate behavioral thermoregulation. The large calcium peaks examined in this study were not observed until approximately one hour into the home cage recording and would have been missed with shorter experiments. The oxytocin system is important for behavioral thermoregulation [41], but the underlying neurobiology has been poorly understood. We identified a distinct pattern of activity where PVN^{OT} neurons are generally "quiet," but display one to a few peaks in the minutes preceding the offset of two resting states (quiescence and quiescent huddle) and in the

seconds following the onset of two active behavioral thermoregulation states occurring within the post-quiescence phase (nesting and active huddle). By uncovering PVN^{OT} dynamics at the rest/wake transition, our finding compliments a study showing that chemogenetic stimulation of PVN^{OT} neurons increases wakefulness and decreases both rapid eye movement (REM) and non-rapid eye movement (NREM) sleep for about an hour [76].

Our recordings were conducted during the resting/light phase, when the mean Tb is approximately 36.6°C in female mice of our colony (this study and also [28]). In solo and paired contexts, PVN^{OT} peaks occurred at Tb of 36.06°C and 36.04°C, respectively, or about 0.5°C below the mean. One interpretation of this result is that 36.05°C is near a lower limit of Tb during the resting state and, when detected, PVN^{OT} neurons signal the transition towards the defended Tb of the active state and therefore thermogenesis [7]. In support of this idea, we found that both locomotion and Tb increased in the minutes following PVN^{OT} peaks. Unlike humans, mice show an ultradian pattern of activity and alternate between active and rest states several times within the light phase [5,7,77]. Several neural populations that promote the transition from sleep to wake have been described [78] could contribute to these alternations. One interesting feature of PVN^{OT} neurons is that they become activated minutes before a discernable transition to an active state.

What is the relationship between ambient conditions and the thermoeffector qualities of PVN^{OT} neurons? First, we found that chemogenetic excitation of PVN^{OT} neurons result in increased Tb at a warm temperature (32°C), but not at cooler temperatures. One possibility is that BAT thermogenesis, which is normally inactive at 32°C, was induced by PVN^{OT} excitation. However, our thermography data suggests that increased Tb was not due to iBAT thermogenesis. PVN^{OT}-mediated thermogenesis may therefore operate via thermogenic effects of muscle, digestion, or thyroid function [4,79–81]. Another possibility is that warm ambient conditions are permissive of PVN^{OT} peaks. Indeed, in the paired context, peaks were enhanced at warmer floor temperatures. In both the solo and paired contexts, PVN^{OT} peaks were found when the animals were in the warm microclimate of the nest. These results suggest that PVN^{OT} activation at the end of a bout of rest signals both a transition towards behavioral arousal and a reduction in warm seeking. Consistent with this idea, we found that PVN^{OT} chemogenetic activation reduced warm seeking. Warm seeking and skin warming are core features of mammalian sleep preparation that result in body cooling (i.e., the "warm bath effect") [9]. Skin-warming activates median and medial preoptic hypothalamic glutamate/NOS1 neurons, which in turn promote non-REM sleep and body cooling [9,82]. A proposed function of these neurons is to facilitate a transition towards a lower Tb balance-point to conserve energy. In contrast to this pre-sleep state, our results suggest that PVN^{OT} neurons could facilitate a "pre-arousal" role by reducing warm seeking and initiating a transition towards a higher Tb balance-point optimal for increased rates of physical activity and muscle contraction [83].

One limitation of our study is that we did not examine OT release from PVN^{OT} neurons. Future studies should attempt to link *in vivo* calcium activity with the endocrinological release of OT. In addition, our findings identify specific behavioral states occurring within a narrow time window (on the order of minutes) in which large PVN^{OT} peaks occur. Our chemogenetic manipulations introduced a long-lasting effect on PVN^{OT} activity, and future studies should examine the effect of more temporally precise manipulations in a closed-loop fashion.

Acknowledgements and Funding
We thank University of Wyoming Sensory Biology Center for input; Robert Carrol for assistance with animal husbandry; members of the Nelson and Bedford laboratory for input; Sean Harrington for coding assistance; the UW Engineering Shop for designing and building hardware. This work is funded by NIH COBRE Grant 5P20GM121310-07.

Resource availability

Lead contact

For further information or requests, contact should be directed towards the lead contact, Adam Nelson (anelso74@uwyo.edu).

Materials availability

This study did not generate any new reagents.

Data and code availability

Raw data and code will be made available on a public repository.

Author contributions

M.V., J.F.R., N.L.B., and A.C.N. designed the study. M.V. and J.F.R. performed the fiber photometry and chemogenetic studies. M.V., J.G.L., B.A., C.P., and A.C.N. performed the histology studies. S.K. and G.J.T. performed code development. N.L.B. and A.C.N secured funding and provided expertise and feedback.

Declaration of Interests

The authors declare no competing interests.

References

1. Nakamura, K., Nakamura, Y., and Kataoka, N. (2022). A hypothalamomedullary network for physiological responses to environmental stresses. Nature Reviews Neuroscience *23*, 35–52. https://doi.org/10.1038/s41583-021-00532-x.

2. Morrison, S.F., and Nakamura, K. (2019). Central Mechanisms for Thermoregulation. Annu. Rev. Physiol. *81*, 285–308. https://doi.org/10.1146/annurev-physiol-020518-114546.

3. Almeida, M.C., Vizin, R.C.L., and Carrettiero, D.C. (2015). Current understanding on the neurophysiology of behavioral thermoregulation. Temperature *2*, 483–490. https://doi.org/10.1080/23328940.2015.1095270.

4. Tran, L.T., Park, S., Kim, S.K., Lee, J.S., Kim, K.W., and Kwon, O. (2022). Hypothalamic control of energy expenditure and thermogenesis. Exp Mol Med *54*, 358–369. https://doi.org/10.1038/s12276-022-00741-z.

5. Blessing, W., and Ootsuka, Y. (2016). Timing of activities of daily life is jaggy: How episodic ultradian changes in body and brain temperature are integrated into this process. Temperature *3*, 371–383. https://doi.org/10.1080/23328940.2016.1177159.

6. Refinetti, R. (2020). Circadian rhythmicity of body temperature and metabolism. Temperature *7*, 321–362. https://doi.org/10.1080/23328940.2020.1743605.

7. Škop, V., Liu, N., Xiao, C., Stinson, E., Chen, K.Y., Hall, K.D., Piaggi, P., Gavrilova, O., and Reitman, M.L. (2024). Beyond day and night: The importance of ultradian rhythms in mouse physiology. Molecular Metabolism *84*, 101946. https://doi.org/10.1016/j.molmet.2024.101946.

8. Romanovsky, A.A. (2018). The thermoregulation system and how it works. In Handbook of Clinical Neurology (Elsevier), pp. 3–43. https://doi.org/10.1016/B978-0-444-63912-7.00001-1.

9. Harding, E.C., Franks, N.P., and Wisden, W. (2020). Sleep and thermoregulation. Current Opinion in Physiology *15*, 7–13. https://doi.org/10.1016/j.cophys.2019.11.008.

10. Zayan, U., Caccialupi Da Prato, L., Muscatelli, F., and Matarazzo, V. (2023). Modulation of the thermosensory system by oxytocin. Front Mol Neurosci *15*, 1075305. https://doi.org/10.3389/fnmol.2022.1075305.

11. Harshaw, C., Leffel, J.K., and Alberts, J.R. (2018). Oxytocin and the warm outer glow: Thermoregulatory deficits cause huddling abnormalities in oxytocin-deficient mouse pups. Hormones and Behavior *98*, 145–158. https://doi.org/10.1016/j.yhbeh.2017.12.007.

12. Nixdorf-Miller, A., Hunsaker, D.M., and Hunsaker Iii, J.C. (2006). Hypothermia and Hyperthermia Medicolegal Investigation of Morbidity and Mortality From Exposure to Environmental Temperature Extremes. Archives of Pathology & Laboratory Medicine *130*, 1297–1304. https://doi.org/10.5858/2006-130-1297-HAHMIO.

13. Refinetti, R. (1999). Relationship between the daily rhythms of locomotor activity and body temperature in eight mammalian species. American Journal of Physiology-Regulatory, Integrative and Comparative Physiology *277*, R1493–R1500. https://doi.org/10.1152/ajpregu.1999.277.5.R1493.

14. Glotzbach, S.F., and Heller, H.C. (1976). Central Nervous Regulation of Body Temperature During Sleep. Science *194*, 537–539. https://doi.org/10.1126/science.973138.

15. Junkins, M.S., Bagriantsev, S.N., and Gracheva, E.O. (2022). Towards understanding the neural origins of hibernation. Journal of Experimental Biology *225*, jeb229542. https://doi.org/10.1242/jeb.229542.

16. Revel, F.G., Herwig, A., Garidou, M.-L., Dardente, H., Menet, J.S., Masson-Pévet, M., Simonneaux, V., Saboureau, M., and Pévet, P. (2007). The circadian clock stops ticking during deep hibernation in the European hamster. Proc. Natl. Acad. Sci. U.S.A. *104*, 13816–13820. https://doi.org/10.1073/pnas.0704699104.

17. Škop, V., Guo, J., Liu, N., Xiao, C., Hall, K.D., Gavrilova, O., and Reitman, M.L. (2023). The metabolic cost of physical activity in mice using a physiology-based model of energy expenditure. Molecular Metabolism *71*, 101699. https://doi.org/10.1016/j.molmet.2023.101699.

18. Škop, V., Guo, J., Liu, N., Xiao, C., Hall, K.D., Gavrilova, O., and Reitman, M.L. (2020). Mouse Thermoregulation: Introducing the Concept of the Thermoneutral Point. Cell Reports *31*, 107501. https://doi.org/10.1016/j.celrep.2020.03.065.

19. Morrison, S., F. (2011). Central neural pathways for thermoregulation. Front Biosci *16*, 74. https://doi.org/10.2741/3677.

20. Feng, C., Wang, Y., Zha, X., Cao, H., Huang, S., Cao, D., Zhang, K., Xie, T., Xu, X., Liang, Z., et al. (2022). Cold-sensitive ventromedial hypothalamic neurons control homeostatic thermogenesis and social interaction-associated hyperthermia. Cell Metabolism *34*, 888-901.e5. https://doi.org/10.1016/j.cmet.2022.05.002.

21. Piñol, R.A., Mogul, A.S., Hadley, C.K., Saha, A., Li, C., Škop, V., Province, H.S., Xiao, C., Gavrilova, O., Krashes, M.J., et al. (2021). Preoptic BRS3 neurons increase body temperature and heart rate via multiple pathways. Cell Metabolism *33*, 1389-1403.e6. https://doi.org/10.1016/j.cmet.2021.05.001.

22. Saper, C.B., and Machado, N.L. (2021). The search for thermoregulatory neurons is heating up. Cell Metabolism *33*, 1269–1271. https://doi.org/10.1016/j.cmet.2021.06.010.

23. Tan, C.L., and Knight, Z.A. (2018). Regulation of Body Temperature by the Nervous System. Neuron *98*, 31–48. https://doi.org/10.1016/j.neuron.2018.02.022.

24. ("Bud") Craig, A.D. (2018). Central neural substrates involved in temperature discrimination, thermal pain, thermal comfort, and thermoregulatory behavior. In Handbook of Clinical Neurology (Elsevier), pp. 317–338. https://doi.org/10.1016/B978-0-444-63912-7.00019-9.

25. Jung, S., Lee, M., Kim, D.-Y., Son, C., Ahn, B.H., Heo, G., Park, J., Kim, M., Park, H.-E., Koo, D.-J., et al. (1998). A forebrain neural substrate for behavioral thermoregulation. Neuron *110*, 266-279.e9. https://doi.org/10.1016/j.neuron.2021.09.039.

26. Yahiro, T., Kataoka, N., and Nakamura, K. (2023). Two Ascending Thermosensory Pathways from the Lateral Parabrachial Nucleus That Mediate Behavioral and Autonomous Thermoregulation. J. Neurosci. *43*, 5221–5240. https://doi.org/10.1523/JNEUROSCI.0643-23.2023.

27. Gordon, C.J. (2012). Thermal physiology of laboratory mice: Defining thermoneutrality. Journal of Thermal Biology *37*, 654–685. https://doi.org/10.1016/j.jtherbio.2012.08.004.

28. Landen, J.G., Vandendoren, M., Killmer, S., Bedford, N.L., and Nelson, A.C. (2024). Huddling substates in mice facilitate dynamic changes in body temperature and are modulated by Shank3b and Trpm8 mutation. Communications Biology *7*, 1186. https://doi.org/10.1038/s42003-024-06781-7.

29. Škop, V., Xiao, C., Liu, N., Gavrilova, O., and Reitman, M.L. (2021). The effects of housing density on mouse thermal physiology depend on sex and ambient temperature. Molecular Metabolism *53*, 101332. https://doi.org/10.1016/j.molmet.2021.101332.

30. Sotelo, M.I., Markunas, C., Kudlak, T., Kohtz, C., Vyssotski, A.L., Rothschild, G., and Eban-Rothschild, A. (2024). Neurophysiological and behavioral synchronization in group-living and sleeping mice. Current Biology *34*, 132-146.e5. https://doi.org/10.1016/j.cub.2023.11.065.

31. Fukumitsu, K., Kaneko, M., Maruyama, T., Yoshihara, C., Huang, A.J., McHugh, T.J., Itohara, S., Tanaka, M., and Kuroda, K.O. (2022). Amylin-Calcitonin receptor signaling in the medial preoptic area mediates affiliative social behaviors in female mice. Nat Commun *13*, 709. https://doi.org/10.1038/s41467-022-28131-z.

32. Morrison, I. (2016). Keep Calm and Cuddle on: Social Touch as a Stress Buffer. Adaptive Human Behavior and Physiology *2*, 344–362. https://doi.org/10.1007/s40750-016-0052-x.

33. Panksepp, J.B., and Lahvis, G.P. (2007). Social reward among juvenile mice. Genes Brain Behav *6*, 661–671. https://doi.org/10.1111/j.1601-183X.2006.00295.x.

34. Rogers, J.F., Vandendoren, M., Prather, J.F., Landen, J.G., Bedford, N.L., and Nelson, A.C. (2024). Neural Cell-types and Circuits Linking Thermoregulation and Social Behavior. Neuroscience & Biobehavioral Reviews, 105667. https://doi.org/10.1016/j.neubiorev.2024.105667.

35. Conceição Furber, E.P.S., Mota, C.M.D., Veytsman, E., Morrison, S.F., and Madden, C.J. (2021). Dopaminergic input from the posterior hypothalamus to the raphe pallidus area inhibits brown adipose tissue thermogenesis. American Journal of Physiology-Regulatory, Integrative and Comparative Physiology *321*, R938–R950. https://doi.org/10.1152/ajpregu.00149.2021.

36. Seoyoung Son, Steffy B. Manjila, Kyra T. Newmaster, Yuan-ting Wu, Daniel J. Vanselow, Matt Ciarletta, Todd E. Anthony, Keith C. Cheng, and Yongsoo Kim (2022). Whole-Brain Wiring Diagram of Oxytocin System in Adult Mice. J. Neurosci. *42*, 5021. https://doi.org/10.1523/JNEUROSCI.0307-22.2022.

37. Besnard, A., and Leroy, F. (2022). Top-down regulation of motivated behaviors via lateral septum sub-circuits. Mol Psychiatry *27*, 3119–3128. https://doi.org/10.1038/s41380-022-01599-3.

38. Rizzi-Wise, C.A., and Wang, D.V. (2021). Putting Together Pieces of the Lateral Septum: Multifaceted Functions and Its Neural Pathways. eNeuro *8*, ENEURO.0315-21.2021. https://doi.org/10.1523/ENEURO.0315-21.2021.

39. Menon, R., Süß, T., Oliveira, V.E.D.M., Neumann, I.D., and Bludau, A. (2022). Neurobiology of the lateral septum: regulation of social behavior. Trends in Neurosciences *45*, 27–40. https://doi.org/10.1016/j.tins.2021.10.010.

40. Da Prato, L.C., Zayan, U., Abdallah, D., Point, V., Schaller, F., Pallesi-Pocachard, E., Montheil, A., Canaan, S., Gaiarsa, J.-L., Muscatelli, F., et al. (2022). Early life oxytocin treatment improves thermo-sensory reactivity and maternal behavior in neonates lacking the autism-associated gene Magel2. Neuropsychopharmacol. *47*, 1901–1912. https://doi.org/10.1038/s41386-022-01313-5.

41. Harshaw, C., Leffel, J.K., and Alberts, J.R. (2018). Oxytocin and the warm outer glow: Thermoregulatory deficits cause huddling abnormalities in oxytocin-deficient mouse pups. Hormones and Behavior *98*, 145–158. https://doi.org/10.1016/j.yhbeh.2017.12.007.

42. Froemke, R.C., and Young, L.J. (2021). Oxytocin, Neural Plasticity, and Social Behavior. Annu. Rev. Neurosci. *44*, 359–381. https://doi.org/10.1146/annurev-neuro-102320-102847.

43. Shamay-Tsoory, S.G., and Abu-Akel, A. (2016). The Social Salience Hypothesis of Oxytocin. Biol Psychiatry *79*, 194–202. https://doi.org/10.1016/j.biopsych.2015.07.020.

44. Fukushima, A., Kataoka, N., and Nakamura, K. (2022). An oxytocinergic neural pathway that stimulates thermogenic and cardiac sympathetic outflow. Cell Reports *40*, 111380. https://doi.org/10.1016/j.celrep.2022.111380.

45. Kasahara, Y., Sato, K., Takayanagi, Y., Mizukami, H., Ozawa, K., Hidema, S., So, K.-H., Kawada, T., Inoue, N., Ikeda, I., et al. (2013). Oxytocin Receptor in the Hypothalamus Is Sufficient to Rescue Normal Thermoregulatory Function in Male Oxytocin Receptor Knockout Mice. Endocrinology *154*, 4305–4315. https://doi.org/10.1210/en.2012-2206.

46. Sutton, A.K., Pei, H., Burnett, K.H., Myers, M.G., Rhodes, C.J., and Olson, D.P. (2014). Control of Food Intake and Energy Expenditure by Nos1 Neurons of the Paraventricular Hypothalamus. J. Neurosci. *34*, 15306–15318. https://doi.org/10.1523/JNEUROSCI.0226-14.2014.

47. Noble, E.E., Billington, C.J., Kotz, C.M., and Wang, C. (2014). Oxytocin in the ventromedial hypothalamic nucleus reduces feeding and acutely increases energy expenditure. American Journal of Physiology-Regulatory, Integrative and Comparative Physiology *307*, R737–R745. https://doi.org/10.1152/ajpregu.00118.2014.

48. Biag, J., Huang, Y., Gou, L., Hintiryan, H., Askarinam, A., Hahn, J.D., Toga, A.W., and Dong, H. (2012). Cyto- and chemoarchitecture of the hypothalamic paraventricular nucleus in the C57BL/6J male mouse: A study of immunostaining and multiple fluorescent tract tracing. J of Comparative Neurology *520*, 6–33. https://doi.org/10.1002/cne.22698.

49. Daniel J. Urban, and Bryan L. Roth (2015). DREADDs (Designer Receptors Exclusively Activated by Designer Drugs): Chemogenetic Tools with Therapeutic Utility. Annual Review of Pharmacology and Toxicology *55*, 399–417. https://doi.org/10.1146/annurev-pharmtox-010814-124803.

50. Musardo, S., Contestabile, A., Knoop, M., Baud, O., and Bellone, C. (2022). Oxytocin neurons mediate the effect of social isolation via the VTA circuits. eLife *11*, e73421. https://doi.org/10.7554/eLife.73421.

51. Zhang, L., Chen, H.-C., Li, B., Cao, J.-X., Su, X.-M., Kang, Y.-T., Gao, L.-P., and Jing, Y.-H. (2024). Oxytocin neurons in the paraventricular nucleus and fear empathy among male mice. jpn *49*, E192–E207. https://doi.org/10.1503/jpn.230125.

52. Abreu-Vieira, G., Xiao, C., Gavrilova, O., and Reitman, M.L. (2015). Integration of body temperature into the analysis of energy expenditure in the mouse. Molecular Metabolism *4*, 461–470. https://doi.org/10.1016/j.molmet.2015.03.001.

53. Maloney, S.K., Fuller, A., Mitchell, D., Gordon, C., and Overton, J.M. (2014). Translating Animal Model Research: Does It Matter That Our Rodents Are Cold? Physiology *29*, 413–420. https://doi.org/10.1152/physiol.00029.2014.

54. Nagai, Y., Miyakawa, N., Takuwa, H., Hori, Y., Oyama, K., Ji, B., Takahashi, M., Huang, X.-P., Slocum, S.T., DiBerto, J.F., et al. (2020). Deschloroclozapine, a potent and selective chemogenetic actuator enables rapid neuronal and behavioral modulations in mice and monkeys. Nature Neuroscience *23*, 1157–1167. https://doi.org/10.1038/s41593-020-0661-3.

55. Manvich, D.F., Webster, K.A., Foster, S.L., Farrell, M.S., Ritchie, J.C., Porter, J.H., and Weinshenker, D. (2018). The DREADD agonist clozapine N-oxide (CNO) is reverse-metabolized to clozapine and produces clozapine-like interoceptive stimulus effects in rats and mice. Sci Rep *8*, 3840. https://doi.org/10.1038/s41598-018-22116-z.

56. Blessing, W., McAllen, R., and McKinley, M. (2016). Control of the Cutaneous Circulation by the Central Nervous System. In Comprehensive Physiology, Y. S. Prakash, ed. (Wiley), pp. 1161–1197. https://doi.org/10.1002/cphy.c150034.

57. Blessing, W.W., Blessing, E.M., Mohammed, M., and Ootsuka, Y. (2017). Clozapine, chlorpromazine and risperidone dose-dependently reduce emotional hyperthermia, a biological marker of salience. Psychopharmacology *234*, 3259–3269. https://doi.org/10.1007/s00213-017-4710-x.

58. Loffler, S., Korber, J., Nubbemeyer, U., and Fehsel, K. (2012). Comment on “Impaired respiratory and body temperature control upon acute serotonergic neuron inhibition.” Science *337*, 646; author reply 646. https://doi.org/10.1126/science.1221810.

59. Nentwig, T.B., Obray, J.D., Vaughan, D.T., and Chandler, L.J. (2022). Behavioral and slice electrophysiological assessment of DREADD ligand, deschloroclozapine (DCZ) in rats. Sci Rep *12*, 6595. https://doi.org/10.1038/s41598-022-10668-0.

60. Claes, M., De Groef, L., and Moons, L. (2022). The DREADDful Hurdles and Opportunities of the Chronic Chemogenetic Toolbox. Cells *11*, 1110. https://doi.org/10.3390/cells11071110.

61. Zhang, Y., Rózsa, M., Liang, Y., Bushey, D., Wei, Z., Zheng, J., Reep, D., Broussard, G.J., Tsang, A., Tsegaye, G., et al. (2023). Fast and sensitive GCaMP calcium indicators for imaging neural populations. Nature *615*, 884–891. https://doi.org/10.1038/s41586-023-05828-9.

62. Resendez, S.L., Namboodiri, V.M.K., Otis, J.M., Eckman, L.E.H., Rodriguez-Romaguera, J., Ung, R.L., Basiri, M.L., Kosyk, O., Rossi, M.A., Dichter, G.S., et al. (2020). Social Stimuli Induce Activation of Oxytocin Neurons Within the Paraventricular Nucleus of the Hypothalamus to Promote Social Behavior in Male Mice. J. Neurosci. *40*, 2282. https://doi.org/10.1523/JNEUROSCI.1515-18.2020.

63. Yukinaga, H., Hagihara, M., Tsujimoto, K., Chiang, H.-L., Kato, S., Kobayashi, K., and Miyamichi, K. (2022). Recording and manipulation of the maternal oxytocin neural activities in mice. Current Biology *32*, 3821-3829.e6. https://doi.org/10.1016/j.cub.2022.06.083.

64. Zhan, S., Qi, Z., Cai, F., Gao, Z., Xie, J., and Hu, J. (2024). Oxytocin neurons mediate stress-induced social memory impairment. Current Biology *34*, 36-45.e4. https://doi.org/10.1016/j.cub.2023.11.037.

65. Endo, N., Ujita, W., Fujiwara, M., Miyauchi, H., Mishima, H., Makino, Y., Hashimoto, L., Oyama, H., Makinodan, M., Nishi, M., et al. (2018). Multiple animal positioning system shows that socially-reared mice influence the social proximity of isolation-reared cagemates. Communications Biology *1*, 225. https://doi.org/10.1038/s42003-018-0213-5.

66. Gordon, C.J., Aydin, C., Repasky, E.A., Kokolus, K.M., Dheyongera, G., and Johnstone, A.F.M. (2014). Behaviorally mediated, warm adaptation: A physiological strategy when mice behaviorally thermoregulate. Journal of Thermal Biology *44*, 41–46. https://doi.org/10.1016/j.jtherbio.2014.06.006.

67. Harding, E.C., Franks, N.P., and Wisden, W. (2019). The Temperature Dependence of Sleep. Front. Neurosci. *13*, 336. https://doi.org/10.3389/fnins.2019.00336.

68. Sotelo, M.I., Tyan, J., Markunas, C., Sulaman, B.A., Horwitz, L., Lee, H., Morrow, J.G., Rothschild, G., Duan, B., and Eban-Rothschild, A. (2022). Lateral hypothalamic neuronal ensembles regulate pre-sleep nest-building behavior. Current Biology *32*, 806-822.e7. https://doi.org/10.1016/j.cub.2021.12.053.

69. De Lecea, L., Carter, M.E., and Adamantidis, A. (2012). Shining Light on Wakefulness and Arousal. Biological Psychiatry *71*, 1046–1052. https://doi.org/10.1016/j.biopsych.2012.01.032.

70. Brownstone, R.M., and Chopek, J.W. (2018). Reticulospinal Systems for Tuning Motor Commands. Front. Neural Circuits *12*, 30. https://doi.org/10.3389/fncir.2018.00030.

71. Engmann, A.K., Bizzozzero, F., Schneider, M.P., Pfyffer, D., Imobersteg, S., Schneider, R., Hofer, A.-S., Wieckhorst, M., and Schwab, M.E. (2020). The Gigantocellular Reticular Nucleus Plays a Significant Role in Locomotor Recovery after Incomplete Spinal Cord Injury. J. Neurosci. *40*, 8292–8305. https://doi.org/10.1523/JNEUROSCI.0474-20.2020.

72. Althammer, F., and Grinevich, V. (2018). Diversity of oxytocin neurones: Beyond magno- and parvocellular cell types? J Neuroendocrinology *30*, e12549. https://doi.org/10.1111/jne.12549.

73. Li, H., Jiang, T., An, S., Xu, M., Gou, L., Ren, B., Shi, X., Wang, X., Yan, J., Yuan, J., et al. (2024). Single-neuron projectomes of mouse paraventricular hypothalamic nucleus oxytocin neurons reveal mutually exclusive projection patterns. Neuron *112*, 1081-1099.e7. https://doi.org/10.1016/j.neuron.2023.12.022.

74. Carcea, I., Caraballo, N.L., Marlin, B.J., Ooyama, R., Riceberg, J.S., Mendoza Navarro, J.M., Opendak, M., Diaz, V.E., Schuster, L., Alvarado Torres, M.I., et al. (2021). Oxytocin neurons enable social transmission of maternal behaviour. Nature *596*, 553–557. https://doi.org/10.1038/s41586-021-03814-7.

75. Tang, Y., Benusiglio, D., Lefevre, A., Hilfiger, L., Althammer, F., Bludau, A., Hagiwara, D., Baudon, A., Darbon, P., Schimmer, J., et al. (2020). Social touch promotes interfemale communication via activation of parvocellular oxytocin neurons. Nature Neuroscience *23*, 1125–1137. https://doi.org/10.1038/s41593-020-0674-y.

76. Chen, C.-R., Zhong, Y.-H., Jiang, S., Xu, W., Xiao, L., Wang, Z., Qu, W.-M., and Huang, Z.-L. (2021). Dysfunctions of the paraventricular hypothalamic nucleus induce hypersomnia in mice. eLife *10*, e69909. https://doi.org/10.7554/eLife.69909.

77. Gordon, C.J. (2012). The mouse: An “average” homeotherm. Journal of Thermal Biology *37*, 286–290. https://doi.org/10.1016/j.jtherbio.2011.06.008.

78. Sulaman, B.A., Wang, S., Tyan, J., and Eban-Rothschild, A. (2023). Neuro-orchestration of sleep and wakefulness. Nat Neurosci *26*, 196–212. https://doi.org/10.1038/s41593-022-01236-w.

79. Calcagno, M., Kahleova, H., Alwarith, J., Burgess, N.N., Flores, R.A., Busta, M.L., and Barnard, N.D. (2019). The Thermic Effect of Food: A Review. Journal of the American College of Nutrition *38*, 547–551. https://doi.org/10.1080/07315724.2018.1552544.

80. Morrison, S.F., Nakamura, K., and Madden, C.J. (2008). Central control of thermogenesis in mammals. Experimental Physiology *93*, 773–797. https://doi.org/10.1113/expphysiol.2007.041848.

81. Silva, J.E. (2003). The Thermogenic Effect of Thyroid Hormone and Its Clinical Implications. Ann Intern Med *139*, 205. https://doi.org/10.7326/0003-4819-139-3-200308050-00010.

82. Harding, E.C., Yu, X., Miao, A., Andrews, N., Ma, Y., Ye, Z., Lignos, L., Miracca, G., Ba, W., Yustos, R., et al. (2018). A Neuronal Hub Binding Sleep Initiation and Body Cooling in Response to a Warm External Stimulus. Current Biology *28*, 2263-2273.e4. https://doi.org/10.1016/j.cub.2018.05.054.

83. Bennett, A.F. (1984). Thermal dependence of muscle function. American Journal of Physiology-Regulatory, Integrative and Comparative Physiology *247*, R217–R229. https://doi.org/10.1152/ajpregu.1984.247.2.R217.

METHODS

Animals

OT and FOS histology. C57B6/J (Strain #: 000664) female mice were purchased from Jackson Laboratory and were 8 to 11 weeks old during the experimental period.

PVN^{OT} manipulation and recording. Oxytocin-Ires-Cre mice were purchased from Jackson Laboratory (Strain #: 024234) (Wu et al., 2012). Animals were bred and maintained at the University of Wyoming. Experimental female mice ranged from 9-20 weeks old during the experimental period.
All experimental mice were group-housed with *ad libitum* access to food and water in a room maintained at 23±2°C with a standard 12 h light / dark cycle (light: 6:00-18:00; dark: 18:00-6:00) until they were used for surgery or experiments. Animals were housed in Optimice® IVC cage systems; cages were enriched with red huts, nestlets, and a mix of cob and pine bedding. Mice used were 18-26g during the experimental period. Animal genotyping was outsourced to Transnetyx using ear tissue biopsies. All procedures were approved by the University of Wyoming Institute Animal Care and Use Committee (IACUC) in compliance with NIH guidelines for the care and use of laboratory animals.

FOS/*Fos* behavior assays

To measure FOS protein expression across brain regions, mice were placed into the home cage recording suite as described (Landen et al., 2024) for at least 24 hours prior to behavior being monitored, with the cage's camera being connected to a Zoom meeting. After the 24 hours, beginning at the start of the light cycle when huddling is most frequent, a human observer monitored behavior from another room, without interrupting natural behavior. Once the target behavior was observed for a minimum of 15 consecutive minutes, 90 minutes were counted from the onset of the behavior, and animals were pulled from the recording suite for histology.

To determine *Fos* transcription in PVN^{OT} neurons during different huddling states, C57B6/J female mice that were 10 weeks old were housed in home cages in trios. Mice were habituated to the conditions, handling, and the cage lid camera set up for ~5 days prior to recording. Animals were split into two groups: active huddle (N=6) and quiescent huddle (N=3). To capture active huddle *Fos* transcription, mice were recorded using the cage lid camera connected to a Zoom meeting. The time of active huddle onset was documented, and mice were sacrificed 30 minutes later. To determine quiescent huddle *Fos* transcription, mice were recorded as described above. Mice were sacrificed 30 minutes after the onset of quiescent or active huddle. All brains were dissected, embedded in OCT (Fisher Scientific, #23-730-571) and stored in -80°C.

Thermal profile

Thermography. For thermographic analysis of the surface of iBAT, Trunk, and Tail, a thermal imaging camera (FLIR, Model: A50 51) was placed above the arena and recorded at one frame/second. Thermal data were manually annotated in the FIJI program ThermImageJ v3.1 (Tattersall, 2019). Approximately 45 frames (a frame every ~20s) were analyzed per recording. Target body regions were manually highlighted (9x9 circular ROI of pixels for iBAT and Trunk, and a 60-pixel linear segment for Tail) at each frame. iBAT loci were identified and scored by highlighting the interscapular region of the mouse, Trunk as the region on the trunk of the animal anterior of the tail, and Tail by using a segmented line started approximately 15 pixels away from the base of the tail. Data was extracted for those highlighted regions including the mean, maximum, and standard deviation of temperature (°C) for each ROI or segment, along with a PC-derived timestamp. These data were then joined with other data streams based on the timestamp. Although we report data for the mean values, we found very similar statistical results when using the max values

Hot/cold plate experiments. To measure effects of PVN^{OT} on thermogenic responses, experimental mice were placed in one of three different floor temperatures for 15 minutes, receiving an i.p. injection of either a saline-based vehicle solution (0.5% molecular grade ethanol in 0.9% sterile sodium chloride) or deschloroclozapine (DCZ) DREADD agonist (0.05mg/mL, Hello Bio HB8555) 15 minutes before the start of the assay. DCZ was delivered at 0.1 mg/Kg. Experimental condition one was 15º (innocuous cold), condition two was 32ºC (innocuous warm) and condition three was 15ºC with pedestal access. The pedestal was ~5 ºC warmer than the plate and was large enough for the mouse to fit its entire trunk over, therefore providing cold-relief. Pedestal access was granted to the mouse at the 10:00 minute point in the assay. Different floor temperature environments were controlled via a Hot/Cold Plate (Ugo Basile, #35300). Immediately after a mouse was placed on the plate, its behavior was recorded via a camera (500W02M-L36, SVPRO) directly above the arena, with physical activity during the assay being quantified via pixel-change using behavioral-analysis software (Ethovision XT16). For pedestal conditional experiments, 'On pedestal' or

'On floor' were manually scored via behavioral analysis software (Ethovision XT 16). Body temperature (T_b) was recorded every second for the duration of the assay via abdominally implanted thermologgers (DST nano-T, STAR-ODDI loggers) and data extracted with Star-Oddi Mercury (v6.5), application software.

Animal Surgery

Pre- and post-surgical procedures.

Prior to surgery, animals were given an analgesic dose of carprofen (20 mg/kg, s.c.). Mice were deeply anesthetized using a mixture of ketamine and xylazine (100 mg/kg and 10 mg/kg, respectively, administered i.p.). Mice were returned to a warm and clean homecage post-surgery. For post-operative care, antibiotic ointment (Neomycin and Polymyxin B Sulfates and Dexamethasone Ophthalmic Ointment, Bausch + Lomb) was topically applied to the incision, animals received 300 µL lactated ringer s.c., and closely observed until active. Once standing, 1 mg/kg of buprenorphine extended-release solution was administered subcutaneously between the shoulder blades.

Temperature logger implants. In order to continuously measure internal body temperature, mice were implanted with Star-Oddi DST nano-T temperature loggers. The loggers were disinfected with glutaraldehyde and rinsed with sterile PBS prior to being implanted intraperitoneally. Mice were anesthetized as described above. A one-centimeter incision was made in the skin and underlying peritoneum. The peritoneum was sutured with PGA absorbable sutures, while the skin was closed with nylon (nonabsorbable) sutures. Mice received post-surgical care as described above. All animals recovered for a minimum of seven days with their cage mates and until visible scarring was gone before being tested.

Stereotaxic DREADD injections. For activation or inactivation of PVN^{OT} neurons,oxytocin-Ires-Cre heterozygous female and male mice underwent stereotaxic injections with AAV5 hSyn-DIO-hM4D(Gi)-mCherry (#44362, Addgene, titer: 2.4 x 10^{13} gc/mL) or hSyn-DIO-hM3D(Gq)-mCherry (#44361, Addgene, titer: 2.6 x 10^{13} gc/mL) at the age of eight weeks. Mice were head-fixed on a digital mouse stereotax (Stoelting, 51730D). For added analgesia, a local anesthetic (5% lidocaine) was delivered subcutaneously along the incision site before cutting. A midline incision was made along the top of the skull, the periosteum was cleared with 3% hydrogen peroxide, and the skull dried off with canned air. Vertical measurements of bregma and lambda were taken and aligned to the same plane (DV of ± 0.05 mm). Viral vectors were delivered using a programmable nanoliter injector, (Nanoject III, Drummond Scientific) (300nL per side: 6 cycles of 50nL delivered at 2nL/s with 10 second delays). To allow for proper diffusion of solution into brain tissue, the needle was left in for 10 minutes before retracting. PVN coordinates relative to bregma and DV measured from the top of the brain: AP = -0.76mm, ML= ±0.19mm, DV= -4.62mm. The incision was closed using absorbable PGA suture threads and antibiotic ointment was applied topically along the incision. Mice recovered for two weeks prior to being tested.

Stereotaxic GCaMP injections and fiber implants. For fiber photometry recordings, oxytocin-Ires-Cre heterozygous, pair-housed, female mice at 8-12 weeks of age underwent stereotaxic injections with pGP-AAV9-syn-FLEX-jGCaMP8s-WPRE (#162377, Addgene, titer: 2.7 x 10^{13} gc/mL) with the same surgical procedure as described above. Two animals received AAV9-Syn-GCaMP6f-WPRE-SV40 (#100837, Addgene, titer: 2.8 x 10^13 gc/mL) and were used in the full analysis of calcium peaks and body temperature. A fiber-optic cannula (Ø1.25mm ferrule, Ø200 µm core, NA = 0.37, L= 6.5 mm, Neurophotometrics Ltd.) was lowered into the injection site until the tip was located ~ 0.02 mm above the viral injection. The cannula was anchored in place with dental cement (C&B Metabond) such that a dome-shaped cap was halfway up the black ceramic ferrule and covered the entire incision. Post-operative care and recovery took place as described above. Two weeks post recovery, animals were tested for GCaMP signal using the Neurophotometrics photometry system (as described in "**Fiber photometry recordings"**). If a signal was detected, animals underwent an additional surgery to abdominally implant a thermologger as described above. Animals with no detectable signal were excluded from recordings.

Stereotaxic CTB and tail vein injections. To identify PVN^{OT} projections to rMR, a subset of hSyn-DIO-hM3D(Gq)-mCherry-expressing mice received a secondary stereotaxic injection of cholera toxin subunit B conjugated with Alexa Fluor 647 (Invitrogen, C34778). Upon completion of behavioral assays, mice underwent an additional stereotaxic surgery in which 10 nL of 0.5% CTB was injected into the rMR. Coordinates relative to bregma and DV measured from the top of the brain: AP = -5.80mm, ML= 0.00mm, DV= -4.95mm. Mice received post-operative care as described above and recovered for 3-4 days. For intravenous labeling of magnocellular and parvocellular OT neurons, mice received 15 uL of 4% Fluoro-Gold (Fluorochrome) diluted in 100 uL of sterile saline. Prior to injection, mice were given an analgesic dose of carprofen (20 mg/kg, s.c.). Mice were briefly restrained using a modified 50 mL conical tube, in

which holes were drilled to allow for proper air flow and respiration. Mouse tails were interposed between two heating pads to enhance visibility of the tail vein. Tails were wiped down with 70% ethanol and FG was administered via either right or left lateral tail vein using a 0.5 mL 28G syringe. Mice were sacrificed 24- 48 hours post-FG administration.

Histology

FOS Immunohistochemistry. For quantitative analysis of FOS expression, mice were given a lethal dose of isoflurane after removal from the home cage recording suite. Animals were then transcardially perfused with 1X PBS and 4% paraformaldehyde (PFA) in PBS. Brains were removed and kept in 4% PFA overnight at 4°C. Brains were sliced into 60 um sections using a vibratome (Leica VT1000S) and every other slice was saved in 48-well plates, wrapped in parafilm in 1X PBS, overnight at 4°C. The next day, 0.3 mL of block solution (0.20% triton, 10% natural goat serum (NGS) (Jackson ImmunoResearch 005-000-121), in 1X PBS) was placed into each well and incubated for one hour at room temperature on a plate shaker. Block was removed and replaced with freshly made primary antibody solution (c-Fos (9F6) Rabbit mAb, Cell Signaling, 14609, 1:1000 dilution in block solution) and incubated for 48 hours on a shaker at 4°C. Slices were washed three times with 1X PBS for 15 minutes. Slices were then incubated in secondary antibody solution (Goat anti-Rabbit IgG, Alexa Fluor Plus 555, Thermo Scientific, A32732, 1:500 dilution in block) for 2 hours on a shaker at room temperature, and protected from light. Wash steps were repeated with 1X PBS. Slices were then mounted on Superfrost Plus slides using a paintbrush, and stained with DAPI mounting medium (Vectashield H-2000). Slides were imaged with a Zeiss Axio Scan.Z1 fluorescent microscope. Regions were identified by finding all locations that displayed FOS expression, and cropped using ImageJ alongside the Allen Brain Atlas. Quantity of cells and overlap was calculated using a custom CellProfiler 4.2.1 script.

Fluorescent *in situ* hybridization (RNAscope)

For quantitative analysis of *Oxt* and *Fos* overlap in PVN^{OT} and *Oxtr* and *Vglut3* in the rMR, mice were anesthetized with a lethal amount of isoflurane. Brains were extracted, embedded in OCT and stored at -80°C. Brains were sectioned at 16 µm using a cryostat and subsequently stored at -80°C until use. Slides containing brain sections were placed in 4% PFA for 45 minutes at room temperature (RT) and then were dehydrated in 50%, 70% and 100% ethanol for 5 minutes each at RT. Once slides dried for 5 minutes after dehydration; hydrogen peroxide was added for 10 minutes at RT. Slides were then treated with Protease III for 30 minutes at RT to allow for antigen accessibility. For the PVN, the probe cocktail was made with *Oxt* (ACD Bio, #493171) and *Fos* (ACD Bio, #316921) and diluted at 1:2 ratio with probe diluent. For rMR sections, the probe cocktail contained *Slc17a8* (ACD Bio, #1199011) and *Oxtr* (ACD Bio, #454011). An aliquot of 40µL of probe cocktail was added to each section and incubated in a 40°C oven for two hours. For amplification, 40µL of AMP 1 was added each slice and placed in the 40°C oven for 15 minutes. AMP 2 was then added to each slice and slides were again incubated at 40°C for 15 minutes. Finally, 2-3 drops of AMP 3 were added to each slice and slides were incubated at 40°C for 30 minutes.

Fluorophores were added to each channel and diluted 1:1500. Each fluorophore was added by first opening the channel using 2-3 drops of HRP on each slice and incubating at 40°C for 15 minutes. Once the channel was opened, the fluorophore was added at a volume of 40 µL to each slice and slides were incubated at 40°C for 30 minutes. To close the channel, 2-3 drops of blocker were added to each slice for and incubated for 15 minutes. Lastly, a drop of DAPI (ACD Bio, #320858**)** was added to each slice for 30-45 seconds. DAPI was allowed to dry for approximately 3 minutes before immediately coverslipping with 1-2 drops of ProLong Gold (Invitrogen, P36930). Slides were protected from any surrounding light, left to dry overnight and imaged with a Zeiss Axio Scan.Z1.

DREADD and GCaMP expression. To verify AAV injection sites, animals who had received stereotaxic DREADD and/or GCaMP8s injections were sacrificed at ≤18 weeks. Mice were deeply anesthetized with a lethal amount of isofluorane and perfused with 4% PFA. Extracted brains were then stored in 4% PFA overnight at 4 before being sliced at 60 µm using a vibratome (Leica VT1000S). PVN and rPa regions were identified via the Allen Brain Atlas. For confirmation of DREADD viral expression, PVN slices were stained with a DAPI mounting medium (200 µl/slide, Vectashield H-2000) and scanned using a Zeiss Axio Scan.Z1.

For GCaMP8s expressing mice, an additional staining protocol of far-red (640) Nissl (N21483, Thermofisher Scientific) was used to both identify the viral expression and characterize the placement of the optic fiber. After initial mounting and drying of PVN slices on slides, they were then rehydrated in PBS before application of the Nissl stain (1:80 dilution, 200 µl/slide). Slides were again washed in PBS and PBST baths, before being left at room temperature overnight and then stained with DAPI before imaging as described above. Images were enhanced and/or pseudo-colored using ImageJ.

Fiber photometry recordings

Recording setup. The Neurophotometrics fiber photometry system (FP3001), operating with Bonsai (Version 2.72) software, was used to acquire photometric data with concurrent video recordings (Arducam, OV9281). Patch cords (MBF Bioscience, NPM-BPC-4) were attached to the fiber ferrules, and held in place by either ceramic sleeves or by a quick-release interconnecter (ThorLabs, ADAL3). Calcium dependent GCaMP (GCaMP6f and GCaMP8s) fluorescence signals were recorded with light from a 470-nm LED that was band-pass filtered, narrowed with a collimator, reflected by a dichroic mirror, and focused on the sensor of a CCD camera by a 20x objective. To account for auto-fluorescence and possible motion artifacts, a 415-nm LED for calcium-independent isosbestic fluorescence signal was used. The recorded signals were acquired with a sampling rate of 30 Hz for each channel at 100% duty cycle. LED light was delivered at a power that resulted in 60 uW of 415-nm light, and 85 uW of 470-nm light at the tip of the patch cord. LED light power was calibrated prior to every recording using a power meter (ThorLabs, PM100USB and S120C).

Photometric recordings occurred in the homecage, with the cage-lid replaced by a custom-fit metal sleeve that extended the cage wall height to 16". Optic fiber-implanted mice and their pair-housed sister were habituated to the connector and patch-cord prior to commencement of experimental schedule. Habituation periods ranged from several days to a week depending on individual animal reaction to the patchcord and to sufficiently aversion train the cagemate. Aversion training was performed during habituation periods by lightly coating the patchcord with diluted capsaicin (EMD Millipore, 211275). The cagemate and implant mouse were observed and training was repeated until the cagemate associated the unpleasant sensation of capsaicin with chewing of the patchcord. Recordings were approximately 2-hours and were conducted at three different floor temperatures (15Cº, 23Cº and 29ºC), with and without the sister cage-mate. Floor temperature was controlled by placing the home-cage onto a custom aluminum chassis that attached to the Hot/Cold Plate, temperature was then validated by a temperature logging iButton (DS1922L-F5, Embedded Data Systems) placed inside the home-cage. A portion of the nesting material was removed before experiments to prevent occlusion of the animals during the recording (see Supplementary Video 1 for typical amount of bedding left in cage).

To validate chemogenetic excitation of PVN^{OT} Fiber implanted mice that also expressed DREADD Gq received an i.p. injection of either vehicle solution or DCZ solution 30 minutes into the recording.

Behavioral characterization. Videos were uploaded to Noldus Ethovision XT 16, where the physical activity of the mice (calculated total percentage of pixel change between frames) and behaviors were identified. Activity in the paired context was defined as the summed activity for both animals.

The behaviors for solo photometry animals were manually scored as follows: Locomotor Activity (LMA), Eating or Drinking (EaDr), Grooming (Groom), Nesting or Nest Building Nest (Nest) where the animal engaged in nest-building behavior or activity within its nest other than grooming, Quiescence (Quies) where the animal is inactive inside its nest, and Stationary (Sta) which was defined as animal inactivity outside of the nest.

The behavior of the photometry animal for paired assays was manually scored as follows: Locomotor Activity (LMA), Eating or Drinking (EaDr), contact initiated (ConI), contact received (ConR), Grooming (Groom), Nesting or Building Nest (Nest) characterized by the photometry animal engaging in nest-building behavior or its activity inside the nest while its cagemate engaged in nest-building behavior, Active huddle (AHud) defined as physical contact and activity between both animals in the nest, Quiescent Huddle (QHud) referred to physical contact and inactivity between both animals in the nest, Quiescence (Quies) where the photometry animal was engaging in inactivity alone in the nest, and Stationary (Sta).

Behavior and activity data was exported at 10 frames per second as a .csv file and imported to R for analysis.

Data preprocessing. Fluorescent signal data preprocessing was done with a custom R script as follows: 415 and 470 channels de-interleaved; 470 channel filtered to remove high-frequency noise using a 4th-order Butterworth filter (Van Boxtel et al., 2021) modified to remove end-effect transients; trimmed to remove approximately the first six minutes of data (to mitigate the effect of photobleaching); if necessary, further trimmed to remove effects of disruptions to the patchcord (chewing or twisting); smoothed with a sliding window function (rollapply; width = 9) (Zeileis et al., 2004).

To correct the calcium-dependent signal from effects of photobleaching and heat-mediated LED decay, we first extracted the "fitted values" from the linear relationship between the 470 (calcium-dependent) and 415 (calcium independent) fluorescent signals. Next, to calculate dF/F we divided the 470 signal by these fitted values. Because we observed occasional artifactual shifts in baseline dF/F values, we baseline corrected dF/F using the iterative least squares method (Liland and Mevik, 2011). The Z-scored dF/F was calculated as $Z = (\chi - \mu)/ \sigma$, where μ is the mean dF/F and σ is the standard deviation of dF/F. To define peaks, we used the findpeaks function (Borchers, 2011), with the minimum peak distance set at two seconds and the minimum peak height set at six standard deviations above the

mean dF/F. Photometric data were aligned to behavioral data (exported from Noldus Ethovision) and Tb data (exported from Mercury) using common centisecond-resolution timestamps and reduced to a sampling frequency of 10 frames per second.

Peri-event data oriented on specific events (i.e., calcium peaks or start/stop frames of behavioral bouts) were extracted using a custom function that (1) extracts the indices of the events and (2) generates a list of vectors for a specified number of rows before and after the event.

Statistics

Effect of behavior state on FOS expression.

To determine the effect of behavior on FOS expression, brain ROIs (divided into left and right sides, where appropriate) were scanned by CellProfiler 4.2.1 to determine the total number of cells, as marked by DAPI. DAPI ROIs were shrunk to a point and then expanded by a factor of 6, and classified as being either FOS-positive or FOS-negative, as marked by presence of the secondary antibody (Alexa Fluor 555), using the same parameters for every slice. These per-ROI portions were then standardized using a Z-score between different histology days, to account for any batch effects of antibody binding or fluorescence. A linear regression model was used on a per-ROI basis, and a post-hoc tukey test was used to determine the effect of behavior on FOS expression, for each brain region. P-values were adjusted for multiple comparisions using the Holm method.

Effect of chemogenetic manipulation on thermal profile.

To determine the effect of PVN^{OT} DREADD manipulation on body temperature, we first explored several different linear mixed-effect models (LMM). In these models, we included physical activity as an independent variable because we observed that DCZ can reduce physical activity. Given that activity and Tb can be correlated, we sought to account for variance in Tb while controlling for correlated effects of activity.

For both inhibitory and excitatory experiments, we used Akaike information criterion (AIC) to determine that an LMM with the highest quality fit of the data utilized (1) an autocorrelation function to account for temporal correlation of measurements and (2) mouseID modeled as a random effect. Specifically, using the nlme package in R, we modeled Tb as a function of drug (DCZ or vehicle), locomotor activity, drug*activity interaction, and time (minutes). A first-order autocorrelation function (corAR1) was included as an independent effect, and mouseID was modeled as a random effect to account for repeated measurements of the same subject. To examine the coefficient estimates of the fixed effects, we used the sjPlot library to generate forest plots (showing confidence intervals unless otherwise noted) and significance values of each fixed effect.

To determine the effect of DREADD manipulation on thermotaxis during cold challenge we used a LMM in R. We modeled “cumulative time spent on pedestal” as a function of drug (DCZ or vehicle), physical activity, and drug*activity interaction. Mouse ID was modeled as a random effect to account for repeated measurements of the same subject. Here again, physical activity was included as a fixed effect because the DCZ compound was observed to affect activity in control experiments. To derive and visualize coefficient estimates of the fixed effects, we used the sjPlot library.

An LMM was again used for thermographic analysis, with temperature being measured as an effect of drug (DCZ) and time. Mouse ID was kept as a random effect and results were correlated using a first-order autocorrelation function (corAR1). As tail results produced a logarithmic curve and were noticed to change more rapidly over the course of the 15-minute assay, we broke the analysis into thirds (0-5, 5-10, 10-15 minutes). P-values were adjusted for multiple comparisions using the Holm method.

Relationship between PVN^{OT} calcium activity and behavior state, activity, and body temperature.

To determine the effect of different behavioral states on calcium peak amplitude and frequency, we fit LMMs with amplitude or frequency as the dependent variable, behavioral state as the independent variable, and mouseID as a random effect. These models were run for both solo and paired conditions.

To determine the effect of social context and floor temperature on calcium peak amplitude and frequency, we fit LMMs with amplitude or frequency as the dependent variable, social context or floor temperature as the independent variable, and mouseID as a random effect.

To determine how calcium peak frequency is affected by behavioral state bout length (i.e., for quiescence and quiescent-huddle) and floor temperature, we fit a LMM with per-bout peak counts as the dependent variable; bout-length, floor temperature, and their interactions as the independent variables; and mouseID as the random effect. We subsequently extracted the standardized beta coefficients using the sjPlot package (Lüdecke, 2013).

To determine how locomotor activity changed during a 300 sec. interval of time surrounding calcium peaks (i.e., peri-peak time), we first z-scored the activity data (estimated at 10 Hz), then smoothed it according to the mean using the rollapply function (Zeileis et al., 2004), and finally calculated the per-second mean for each individual. Next,

we calculated normalized activity data across the 600 sec interval, including the mean normalized activity before and after each peak (i.e., “before-after”). Last, we fit a LMM with normalized activity as the dependent variable, “before-after” as the independent variable, and mouse-ID as a random effect.

To determine peak probability during defined behaviors we used logistic regression. First, we used custom R code to (1) extract the onset and offset of behavioral bouts, and (2) label rows of data (at 10 frames per second) according to whether they occurred within a minute containing (or not containing) a calcium peak (i.e., PeakMinute). Next, we fit a binomial generalized linear model with PeakMinute as the dependent variable; the independent variable was the time span before, during, and after the behavioral epoch of interest (e.g., quiescence offset). Next, we extracted the per-frame predicted values (including standard error) from this model.

To compare the statistical distributions of Tb during calcium peaks *vs*. baseline, we plotted Tb according to the PeakMinute designation described above. We then used a LMM with Tb as the dependent variable; the independent variables were PeakMinute and mouseID as a random effect.

References

Borchers HW. 2011. pracma: Practical Numerical Math Functions. doi:10.32614/CRAN.package.pracma

Landen JG, Vandendoren M, Killmer S, Bedford NL, Nelson AC. 2024. Huddling substates in mice facilitate dynamic changes in body temperature and are modulated by Shank3b and Trpm8 mutation. *Communications Biology* **7**:1186. doi:10.1038/s42003-024-06781-7

Liland KH, Mevik B-H. 2011. baseline: Baseline Correction of Spectra. doi:10.32614/CRAN.package.baseline

Lüdecke D. 2013. sjPlot: Data Visualization for Statistics in Social Science. doi:10.32614/CRAN.package.sjPlot

Tattersall G. 2019. gtatters/ThermImageJ: ThermImageJ. doi:10.5281/ZENODO.2652896

Van Boxtel G, Short T, Kienzle P. 2021. gsignal: Signal Processing. doi:10.32614/CRAN.package.gsignal

Wu Z, Xu Y, Zhu Y, Sutton AK, Zhao R, Lowell BB, Olson DP, Tong Q. 2012. An Obligate Role of Oxytocin Neurons in Diet Induced Energy Expenditure. *PLOS ONE* **7**:e45167. doi:10.1371/journal.pone.0045167

Zeileis A, Grothendieck G, Ryan JA. 2004. zoo: S3 Infrastructure for Regular and Irregular Time Series (Z’s Ordered Observations). doi:10.32614/CRAN.package.zoo

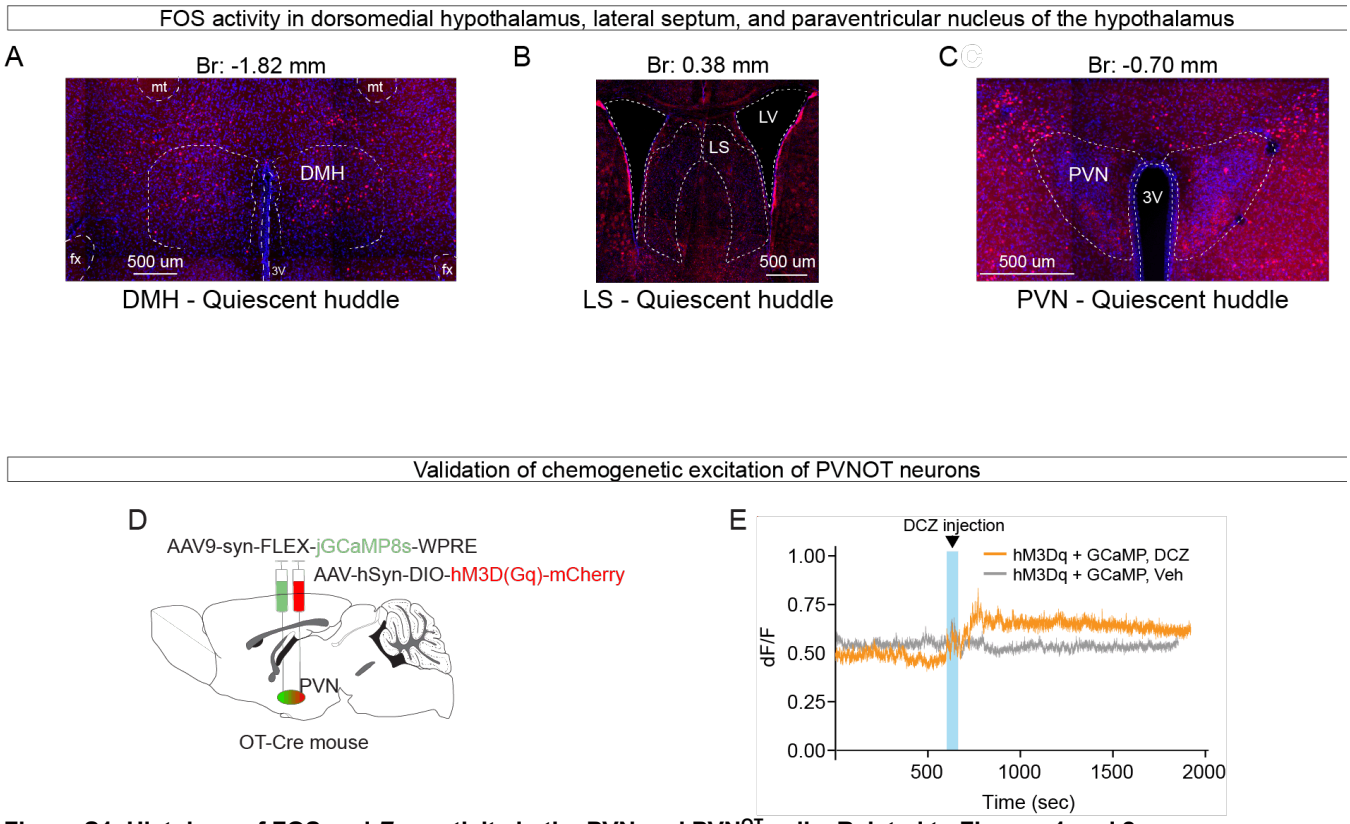

Figure S1. Histology of FOS and *Fos* activity in the PVN and PVN^{OT} cells. Related to Figures 1 and 2.
(A - C) Representative histology images showing quiescent huddling associated FOS expression in the DMH **(A)**, LS **(B)**, and PVN **(C)**. 3V: third ventricle; mt: mammillothalamic tract.
(D) Scheme of GCaMP and excitatory DREADD injections to the PVN of OT-Cre mice.
(E) Photometry recordings of GCaMP signals in the same mouse during vehicle injections and DCZ injections.

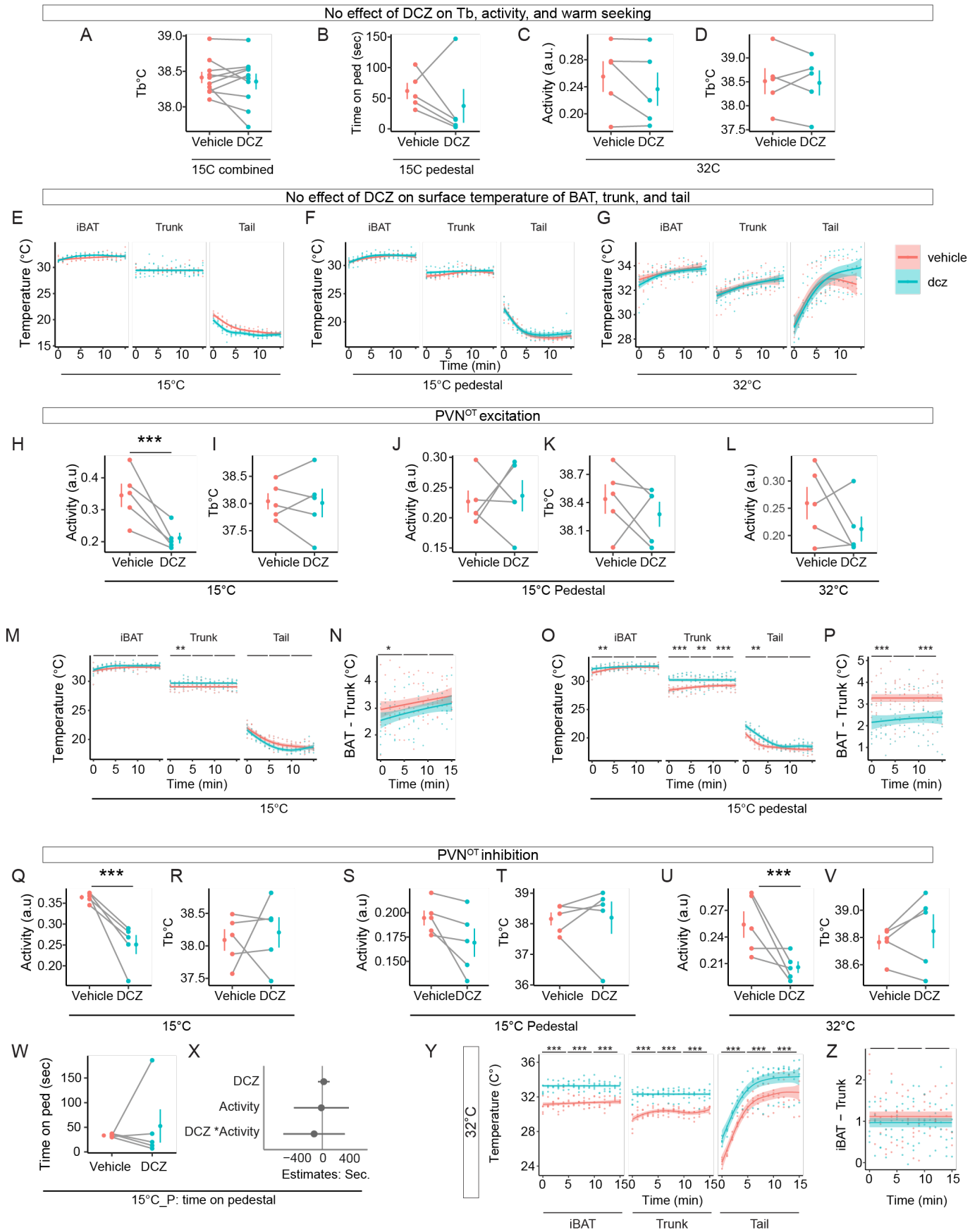

Figure S2. Effects of DZC and PVN^{OT} chemogenetic inhibition on core body temperature, warm seeking, and peripheral vasodilation in female mice. Related to Figure 2.

Fig.2 cont'd.
(A - D) Effect of DCZ on Tb, activity, and time on pedestal. Effect of DCZ (compared to vehicle) on core Tb in the combined 15°C experiments **(A)**, time on pedestal in the 15°C_pedestal experiment **(B)**, physical activity in the 32°C experiment **(C)**, and core Tb in the 32°C experiment **(D)**.
(E - G) Effect of DCZ (compared to vehicle) on surface temperature. Effect of DCZ on the surface temperature of iBAT, trunk, tail, and the iBAT-trunk difference over time in the 15°C **(E)**, 15°C_pedestal experiment **(F)**, and the 32°C experiment **(G)**. Solid lines show mean temperature with shaded areas depicting standard error. Significance is derived from a LMM model to determine effect of drug and time on temperature, with an autocorrelation function to account for temporal correlation of measurements. P-values are adjusted for multiple corrections using the Holm method.
(H - L) Effect of PVN^{OT} excitation on activity and core Tb. Effect of PVN^{OT} excitation on activity **(H)** and core Tb **(I)** in the 15°C experiment. Effect of PVN^{OT} excitation on activity **(J)** and core Tb **(K)** in the 15°C_pedestal experiment. Effect of PVN^{OT} excitation on activity **(L)** in the 32°C experiment.
(M - P) Effect of PVN^{OT} excitation on surface temperature. Effect of PVN^{OT} excitation on iBAT, trunk, and tail **(M)** and iBAT-Trunk **(N)** in the 15°C experiment. Effect of PVN^{OT} excitation on iBAT, trunk, and tail **(O)** and iBAT-Trunk **(P)** in the 15°C_pedestal experiment.
(Q - V) Effect of PVN^{OT} inhibition on activity and core Tb. Effect of PVN^{OT} inhibition on activity **(Q)** and core Tb **(R)** in the 15°C experiment. Effect of PVN^{OT} inhibition on activity **(S)** and core Tb **(T)** in the 15°C_pedestal experiment. Effect of PVN^{OT} inhibition on activity **(U)** and core Tb **(V)** in the 32°C experiment.
(W - X) Effect of PVN^{OT} inhibition on warm seeking. No effect of inhibition on time spent on pedestal **(W)**, including when controlling for

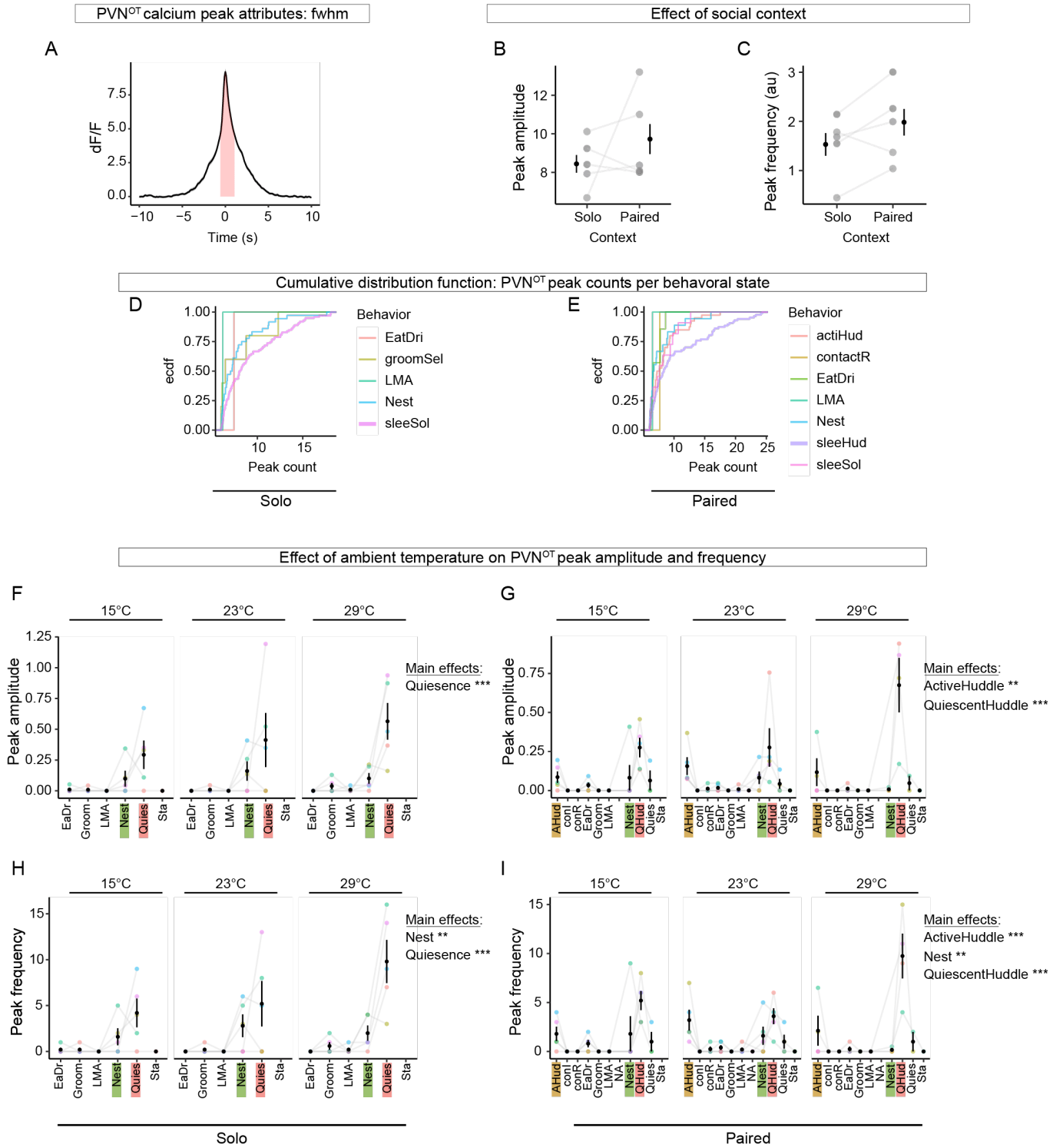

Figure S3. Characterization of PVN^{OT} peaks and their associations with behavioral states. Related to Figure 3.
(A) The mean of normalized PVN^{OT} peaks across conditions. Light red shaded area shows the full width half maximum (1.63 seconds).
(B - C) Effect of social context on PVN^{OT} peaks. PVN^{OT} amplitude **(B)** and peak frequency **(C)** according to social condition.
(D - E) PVN^{OT} empirical cumulative distribution functions (ecdf). Cumulative distribution of peaks for solo **(D)** and paired **(E)** conditions.
(F - G) Effect of floor temperature on PVN^{OT} peak amplitude. Relationship between floor temperature and behavior state in solo **(F)** and paired **(G)** females.

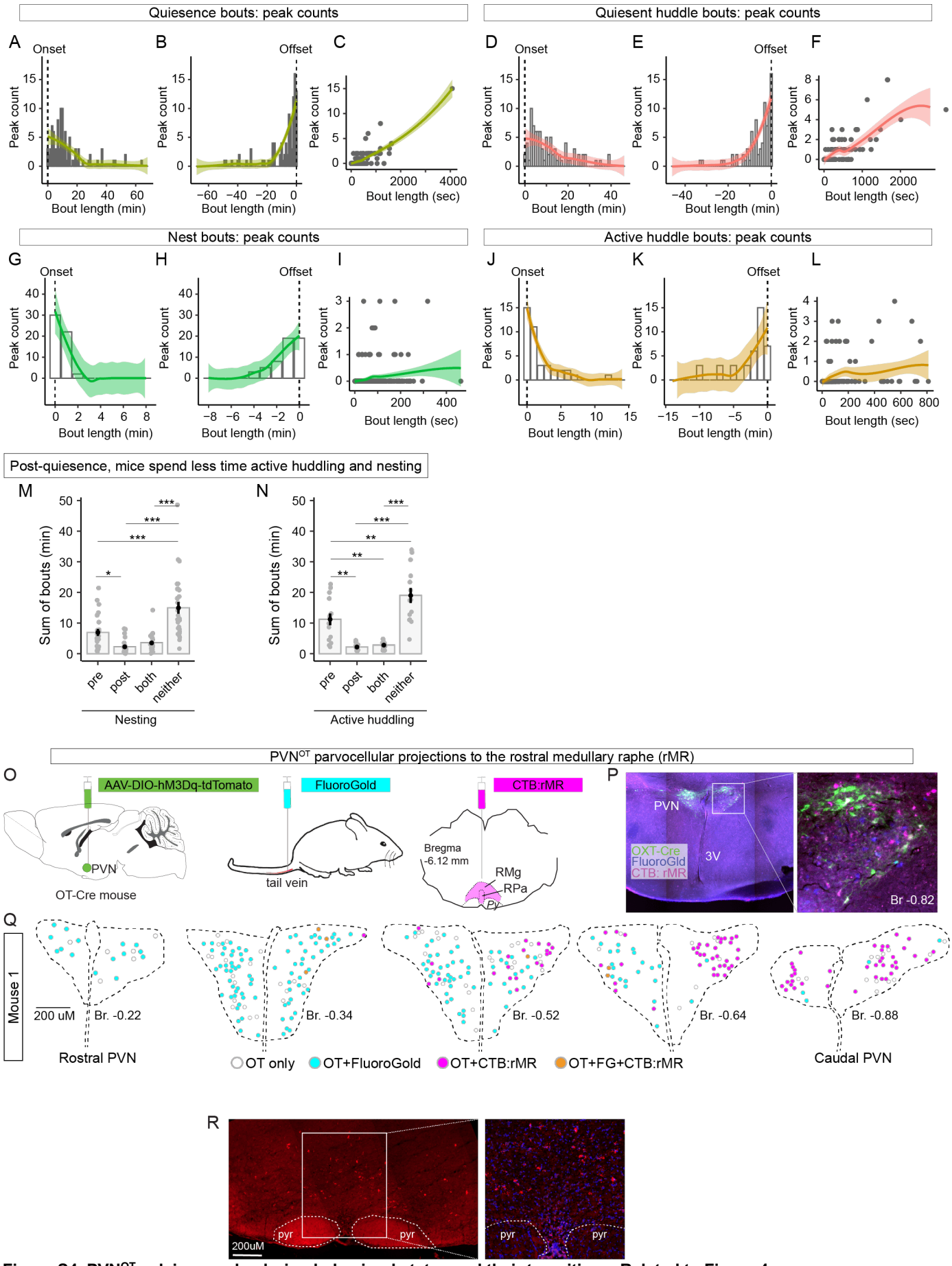

Figure S4. PVN^{OT} calcium peaks during behavioral states and their transitions. Related to Figure 4.

Fig. S4 cont'd.
(A - C) Peak counts for bouts of quiescence. Peak counts aligned to bout onset **(A)**. Peak counts aligned to bout offset **(B)**. Relationship between bout length and peak count **(C)**.
(D - F) Peak counts for bouts of quiescent huddling. Peak counts aligned to bout onset **(D)**. Peak counts aligned to bout offset **(E)**. Relationship between bout length and peak count **(F)**.
(G - I) Peak counts for bouts of nesting. Peak counts aligned to bout onset **(G)**. Peak counts aligned to bout offset **(H)**. Relationship between bout length and peak count **(I)**.
(J - L) Peak counts for bouts of active huddling. Peak counts aligned to bout onset **(J)**. Peak counts aligned to bout offset **(K)**. Relationship between bout length and peak count **(L)**.
(M - N) Sum of bouts according to the phase of quiescence. "Neither" refers to bouts that did not adjoin bouts of quiescence. Nesting bouts **(M)**. Active hudding bouts **(N)**.
(O-P) Microclimate thermal conditions during post quiescence in the paired context. Two mice in active huddling **(O)**. Mean temperatures of the warmest observable temperature in the point of concact during active huddling, the nest, and the floor (experiments at room temperature) **(P)**.
(Q-S) PVN^{OT} parvocellular projections to the rostral medullary raphe (rMR). Scheme of injections to label magno- and parvo-cellular OT neurons **(Q)**. Representative histology showing cells labeled for OXT-Cre, FluoroGold, and CTB **(R)**. Distribution of PVN^{OT} neurons retrogradely labeled with FluoroGold and CTB. Each map was made from one coronal section. Cells double-labeled with FluoroGold and OT-Cre were mostly distributed in the rostral part of the PVN; cells double-labeled with CTB and OT-Cre were in the caudal part of the PVN **(S)**. Fluorescent in situ hybridization of OXTR in the rMR region. Statistical results are from linear mixed models. N = 5

Table S1

	Group	Model	Dep. Variable	Ind. Variable	Rndm effect	DF	T value	P-Val.
Fig. 1C								P-adj.
AHN	AH - QH	Linear	%FOS(Z-score)	Behavior	NA	78	5.09	0.000
AHN	AH - SG	Linear	%FOS(Z-score)	Behavior		78	0.60	1.000
AHN	QH - SG	Linear	%FOS(Z-score)	Behavior		78	-3.30	0.146
ArcHN	AH - QH	Linear	%FOS(Z-score)	Behavior		50	3.29	0.173
ArcHN	AH - SG	Linear	%FOS(Z-score)	Behavior		50	2.92	0.422
ArcHN	QH - SG	Linear	%FOS(Z-score)	Behavior		50	-0.45	1.000
COLL	AH - QH	Linear	%FOS(Z-score)	Behavior		59	1.06	1.000
COLL	AH - SG	Linear	%FOS(Z-score)	Behavior		59	2.26	1.000
COLL	QH - SG	Linear	%FOS(Z-score)	Behavior		59	1.33	1.000
DmHN	**AH - QH**	**Linear**	**%FOS(Z-score)**	**Behavior**		64	5.80	**0.000**
DmHN	**AH - SG**	**Linear**	**%FOS(Z-score)**	**Behavior**		64	4.43	**0.004**
DmHN	QH - SG	Linear	%FOS(Z-score)	Behavior		64	-0.68	1.000
LH	AH - QH	Linear	%FOS(Z-score)	Behavior		150	12.72	0.000
LH	AH - SG	Linear	%FOS(Z-score)	Behavior		150	2.73	0.568
LH	QH - SG	Linear	%FOS(Z-score)	Behavior		150	-7.94	0.000
LPO	AH - QH	Linear	%FOS(Z-score)	Behavior		139	11.43	0.000
LPO	AH - SG	Linear	%FOS(Z-score)	Behavior		139	3.28	0.136
LPO	QH - SG	Linear	%FOS(Z-score)	Behavior		139	-7.13	0.000
LSR	**AH - QH**	**Linear**	**%FOS(Z-score)**	**Behavior**		105	11.28	**0.000**
LSR	**AH - SG**	**Linear**	**%FOS(Z-score)**	**Behavior**		105	7.33	**0.000**
LSR	QH - SG	Linear	%FOS(Z-score)	Behavior		105	-2.87	0.418
MamN	AH - QH	Linear	%FOS(Z-score)	Behavior		125	6.91	0.000
MamN	AH - SG	Linear	%FOS(Z-score)	Behavior		125	2.18	1.000
MamN	QH - SG	Linear	%FOS(Z-score)	Behavior		125	-4.32	0.004
MePO	AH - QH	Linear	%FOS(Z-score)	Behavior		46	2.39	1.000
MePO	AH - SG	Linear	%FOS(Z-score)	Behavior		46	0.43	1.000
MePO	QH - SG	Linear	%FOS(Z-score)	Behavior		46	-1.80	1.000
MPO	AH - QH	Linear	%FOS(Z-score)	Behavior		53	2.46	1.000
MPO	AH - SG	Linear	%FOS(Z-score)	Behavior		53	0.52	1.000
MPO	QH - SG	Linear	%FOS(Z-score)	Behavior		53	-1.67	1.000
PAG	AH - QH	Linear	%FOS(Z-score)	Behavior		101	10.15	0.000
PAG	AH - SG	Linear	%FOS(Z-score)	Behavior		101	-0.18	1.000
PAG	QH - SG	Linear	%FOS(Z-score)	Behavior		101	-9.64	0.000
PH	AH - QH	Linear	%FOS(Z-score)	Behavior		99	10.96	0.000
PH	AH - SG	Linear	%FOS(Z-score)	Behavior		99	3.07	0.249
PH	QH - SG	Linear	%FOS(Z-score)	Behavior		99	-6.79	0.000
PVN	**AH - QH**	**Linear**	**%FOS(Z-score)**	**Behavior**		101	5.42	**0.000**
PVN	**AH - SG**	**Linear**	**%FOS(Z-score)**	**Behavior**		101	4.52	**0.002**
PVN	QH - SG	Linear	%FOS(Z-score)	Behavior		101	-0.08	1.000
SCN	AH - QH	Linear	%FOS(Z-score)	Behavior		78	2.41	1.000
SCN	AH - SG	Linear	%FOS(Z-score)	Behavior		78	0.94	1.000
SCN	QH - SG	Linear	%FOS(Z-score)	Behavior		78	-1.02	1.000
SON	AH - QH	Linear	%FOS(Z-score)	Behavior		56	2.33	1.000
SON	AH - SG	Linear	%FOS(Z-score)	Behavior		56	1.51	1.000
SON	QH - SG	Linear	%FOS(Z-score)	Behavior		56	-0.50	1.000
SubTN	AH - QH	Linear	%FOS(Z-score)	Behavior		60	3.17	0.222
SubTN	AH - SG	Linear	%FOS(Z-score)	Behavior		60	0.72	1.000
SubTN	QH - SG	Linear	%FOS(Z-score)	Behavior		60	-1.72	1.000
TubN	AH - QH	Linear	%FOS(Z-score)	Behavior		55	2.69	0.705
TubN	AH - SG	Linear	%FOS(Z-score)	Behavior		55	2.62	0.818
TubN	QH - SG	Linear	%FOS(Z-score)	Behavior		55	-0.31	1.000
VmHN	AH - QH	Linear	%FOS(Z-score)	Behavior		57	4.07	0.016

VmHN	AH - SG	Linear	%FOS(Z-score)	Behavior		57	1.69	1.000
VmHN	QH - SG	Linear	%FOS(Z-score)	Behavior		57	-2.06	1.000
Figure 1I								
	dorAH - venAH	lmer/Tukey	% *Fos*	Region*behavi	mouseID	27.54	4.31	0.001
	dorAH - dorQH	lmer/Tukey	% *Fos*	Region*behavi	mouseID	8.74	3.30	0.039
	dorAH - venQH	lmer/Tukey	% *Fos*	Region*behavi	mouseID	8.74	1.81	0.333
	venAH - dorQH	lmer/Tukey	% *Fos*	Region*behavi	mouseID	8.59	0.23	0.996
	venAH - venQH	lmer/Tukey	% *Fos*	Region*behavi	mouseID	8.59	-1.30	0.587
	dorQH - venQH	lmer/Tukey	% *Fos*	Region*behavi	mouseID	27.17	-1.52	0.438

	Group	Model	Dep. Variable	Ind. Variable	Rndm effect	DF	T value	P-Val.
Fig. 2G								
	DCZ control experiment		Activity norm.	Intercept	MouseID	14.23	18.11	0.000
	DCZ control experiment		Activity norm.	Drug	MouseID	9.00	-2.99	0.015
Fig. 2H-J								
	15°C	corAR1	Body temp (°C)	Drug	MouseID	137.00	0.50	0.619
	15°C	corAR1	Body temp (°C)	Activity norm.	MouseID	137.00	1.01	0.312
	15°C	corAR1	Body temp (°C)	Minute	MouseID	137.00	3.25	0.001
	15°C	corAR1	Body temp (°C)	Drug:Activity	MouseID	137.00	0.87	0.384
	15°C_Ped	corAR1		drugDCZ		141.00	-1.58	0.116
	15°C_Ped	corAR1		ActivityMM_Mean		141.00	-0.55	0.584
	15°C_Ped	corAR1		Minute		141.00	1.41	0.159
	15°C_Ped	corAR1		drugDCZ:ActivityMM_Mean		141.00	0.41	0.682
	32°C	corAR1		drugDCZ		141.00	2.51	0.013
	32°C	corAR1		ActivityMM_Mean		141.00	0.29	0.769
	32°C	corAR1		Minute		141.00	1.36	0.177
	32°C	corAR1		drugDCZ:ActivityMM_Mean		141.00	-0.04	0.966
Fig. 2K-L								
	Ambient 32°C	corAR1	Body temp (°C)	Drug	MouseID	141.00	2.51	0.013
	Ambient 32°C	corAR1	Body temp (°C)	Activity norm.	MouseID	141.00	0.29	0.769
	Ambient 32°C	corAR1	Body temp (°C)	Time (min)	MouseID	141.00	1.36	0.177
	Ambient 32°C	corAR1	Body temp (°C)	Drug:Activity	MouseID	141.00	-0.04	0.966
Fig. 2O								
	15°C_Ped	lmer	Time on ped	Drug	MouseID	3.97	-2.91	0.044
	15°C_Ped	lmer	Time on ped	Activity norm.	MouseID	3.61	-2.04	0.118
	15°C_Ped	lmer	Time on ped	Drug:Activity	MouseID	4.00	2.11	0.103
Fig. 2P-S								P-adj
	15_F_BAT_Mean_1	corAR1	Surface temp	Drug	MouseID	42.00	1.37	1.000
	15_F_BAT_Mean_2	corAR1	Surface temp	Drug	MouseID	39.00	1.92	1.000
	15_F_BAT_Mean_3	corAR1	Surface temp	Drug	MouseID	46.00	2.87	0.627
	15_F_Rump_Mean_1	corAR1	Surface temp	Drug	MouseID	42.00	-2.07	1.000
	15_F_Rump_Mean_1	corAR1	Surface temp	Drug	MouseID	42.00	4.66	0.004
	15_F_Rump_Mean_2	corAR1	Surface temp	Drug	MouseID	39.00	-1.26	1.000
	15_F_Rump_Mean_2	corAR1	Surface temp	Drug	MouseID	39.00	3.14	0.341
	15_F_Rump_Mean_3	corAR1	Surface temp	Drug	MouseID	46.00	-1.21	1.000
	15_F_Rump_Mean_3	corAR1	Surface temp	Drug	MouseID	46.00	3.26	0.231
	15_F_Tail_Mean_1	corAR1	Surface temp	Drug	MouseID	41.00	-2.53	1.000
	15_F_Tail_Mean_2	corAR1	Surface temp	Drug	MouseID	39.00	-3.41	0.174
	15_F_Tail_Mean_3	corAR1	Surface temp	Drug	MouseID	45.00	-0.79	1.000
	15P_F_BAT_Mean_1	corAR1	Surface temp	Drug	MouseID	42.00	4.43	0.008
	15P_F_BAT_Mean_2	corAR1	Surface temp	Drug	MouseID	40.00	1.63	1.000
	15P_F_BAT_Mean_3	corAR1	Surface temp	Drug	MouseID	52.00	1.15	1.000
	15P_F_Rump_Mean_1	corAR1	Surface temp	Drug	MouseID	42.00	-6.39	0.000
	15P_F_Rump_Mean_1	corAR1	Surface temp	Drug	MouseID	42.00	8.68	0.000
	15P_F_Rump_Mean_2	corAR1	Surface temp	Drug	MouseID	40.00	-3.16	0.327

15P_F_Rump_Mean_2	corAR1	Surface temp	Drug	MouseID	40.00	4.44	0.008
15P_F_Rump_Mean_3	corAR1	Surface temp	Drug	MouseID	52.00	-6.68	0.000
15P_F_Rump_Mean_3	corAR1	Surface temp	Drug	MouseID	52.00	11.64	0.000
15P_F_Tail_Mean_1	corAR1	Surface temp	Drug	MouseID	41.00	4.74	0.003
15P_F_Tail_Mean_2	corAR1	Surface temp	Drug	MouseID	40.00	2.90	0.623
15P_F_Tail_Mean_3	corAR1	Surface temp	Drug	MouseID	52.00	2.61	1.000
32_F_BAT_Mean_1	corAR1	Surface temp	Drug	MouseID	43.00	1.12	1.000
32_F_BAT_Mean_2	corAR1	Surface temp	Drug	MouseID	41.00	2.83	0.712
32_F_BAT_Mean_3	corAR1	Surface temp	Drug	MouseID	50.00	1.33	1.000
32_F_Rump_Mean_1	corAR1	Surface temp	Drug	MouseID	43.00	-4.22	0.015
32_F_Rump_Mean_1	corAR1	Surface temp	Drug	MouseID	43.00	11.27	0.000
32_F_Rump_Mean_2	corAR1	Surface temp	Drug	MouseID	41.00	-2.52	1.000
32_F_Rump_Mean_2	corAR1	Surface temp	Drug	MouseID	41.00	4.67	0.004
32_F_Rump_Mean_3	corAR1	Surface temp	Drug	MouseID	50.00	-2.65	1.000
32_F_Rump_Mean_3	corAR1	Surface temp	Drug	MouseID	50.00	3.31	0.195
32_F_Tail_Mean_1	corAR1	Surface temp	Drug	MouseID	42.00	0.95	1.000
32_F_Tail_Mean_2	corAR1	Surface temp	Drug	MouseID	40.00	12.79	0.000
32_F_Tail_Mean_3	corAR1	Surface temp	Drug	MouseID	49.00	5.93	0.000

	Group	Model	Dep. Variable	Ind. Variable	Rndm effect	DF	T value	P-Val.
Fig. 3F								
	EatDrink	lmer	Amplitude	Behavior	mouseID	19.98	0.08	0.933
	Groom	lmer	Amplitude	Behavior	mouseID	19.98	0.30	0.766
	LMA	lmer	Amplitude	Behavior	mouseID	19.98	0.05	0.963
	Nest	lmer	Amplitude	Behavior	mouseID	19.98	1.99	0.060
	Quiescent	lmer	Amplitude	Behavior	mouseID	19.98	6.84	0.000
	Stationary	lmer	Amplitude	Behavior	mouseID	19.98	0.05	0.962
Fig. 3G								
	EatDrink	lmer	Frequency	Behavior	mouseID	19.86	0.12	0.909
	Groom	lmer	Frequency	Behavior	mouseID	19.86	0.39	0.704
	LMA	lmer	Frequency	Behavior	mouseID	19.86	0.08	0.939
	Nest	lmer	Frequency	Behavior	mouseID	19.86	2.52	0.020
	Quiescent	lmer	Frequency	Behavior	mouseID	19.86	7.44	0.000
	Stationary	lmer	Frequency	Behavior	mouseID	19.91	0.12	0.909
Fig. 3I								
	Active huddle	lmer	Amplitude	Behavior	mouseID	36.00	4.02	0.000
	Contact_Init	lmer	Amplitude	Behavior	mouseID	36.00	0.00	1.000
	Contact_Rec	lmer	Amplitude	Behavior	mouseID	36.00	0.07	0.945
	EatDrink	lmer	Amplitude	Behavior	mouseID	36.00	0.73	0.470
	Groom	lmer	Amplitude	Behavior	mouseID	36.00	0.00	1.000
	LMA	lmer	Amplitude	Behavior	mouseID	36.00	0.08	0.938
	NA	lmer	Amplitude	Behavior	mouseID	36.00	0.00	1.000
	Nest	lmer	Amplitude	Behavior	mouseID	36.00	1.74	0.090
	Quiscent huddle	lmer	Amplitude	Behavior	mouseID	36.00	11.43	0.000
	Quiescent	lmer	Amplitude	Behavior	mouseID	36.00	1.48	0.147
	Stationary	lmer	Amplitude	Behavior	mouseID	36.00	0.00	1.000
Fig. 3J								
	Active huddle	lmer	Amplitude	Behavior	mouseID	36.00	5.37	0.000
	Contact_Init	lmer	Amplitude	Behavior	mouseID	36.00	0.00	1.000
	Contact_Rec	lmer	Amplitude	Behavior	mouseID	36.00	0.10	0.920
	EatDrink	lmer	Amplitude	Behavior	mouseID	36.00	1.14	0.261
	Groom	lmer	Amplitude	Behavior	mouseID	36.00	0.00	1.000
	LMA	lmer	Amplitude	Behavior	mouseID	36.00	0.13	0.894
	NA	lmer	Amplitude	Behavior	mouseID	36.00	0.00	1.000
	Nest	lmer	Amplitude	Behavior	mouseID	36.00	2.42	0.021

	Quiscent huddle	lmer	Amplitude	Behavior	mouseID	36.00	11.95	0.000
	Quiescent	lmer	Amplitude	Behavior	mouseID	36.00	1.95	0.059
	Stationary	lmer	Amplitude	Behavior	mouseID	36.00	0.00	1.000
Fig. 3K							statistic	
	Ta_15 - Ta_23	lmer/Tukey	Frequency	AmbientTemp	mouseID	9.00	-0.80	0.715
	Ta_15 - Ta_29	lmer/Tukey	Frequency	AmbientTemp	mouseID	9.06	-4.16	0.006
	Ta_23 - Ta_29	lmer/Tukey	Frequency	AmbientTemp	mouseID	9.06	-3.34	0.021
Fig. 3K								
	Ta_15 - Ta_23	lmer/Tukey	Frequency	AmbientTemp	mouseID	8.01	-0.30	0.953
	Ta_15 - Ta_29	lmer/Tukey	Frequency	AmbientTemp	mouseID	8.26	-3.52	0.018
	Ta_23 - Ta_29	lmer/Tukey	Frequency	AmbientTemp	mouseID	8.26	-3.24	0.028

	Group	Model	Dep. Variable	Ind. Variable	Rndm effect	DF	T value	P-Val.
Fig. 4C								
	(Intercept)	lmer	Activity norm.	Before/After	MouseID	5.55	-3.67	0.012
	SOLO	lmer				4.00	3.38	0.028
Fig. 4E								
	(Intercept)	lmer	Activity norm.	Before/After	MouseID	4.49	-4.05	0.012
	PAIRED	lmer			MouseID	4.00	4.05	0.015
Fig. 4L								
Nesting	Pre-quies.	lmer	PeakFreq	Quies.Phase	MouseID	25.57	1.67	0.106
	Post-quies.	lmer	PeakFreq	Quies.Phase	MouseID	29.33	3.00	0.005
	Pre and Post	lmer	PeakFreq	Quies.Phase	MouseID	19.80	1.62	0.121
	Neither	lmer	PeakFreq	Quies.Phase	MouseID	5.73	2.20	0.072
Fig. 4O								
Act.Huddle	Pre-quies.	lmer	PeakFreq	Quies.Phase	MouseID	84.39	0.57	0.573
	Post-quies.	lmer	PeakFreq	Quies.Phase	MouseID	56.15	3.38	0.001
	Pre and Post	lmer	PeakFreq	Quies.Phase	MouseID	21.17	1.07	0.295
	Neither	lmer	PeakFreq	Quies.Phase	MouseID	15.90	3.33	0.004
Fig. 4P								
Solo Tb	(Intercept)	lmer	BodyTemp	PeakType	MouseID	1.00	328.84	0.002
	Peak: binary	lmer	BodyTemp	PeakType	MouseID	396246.02	-37.88	0.000
Fig. 4R								
Paired Tb	(Intercept)	lmer	BodyTemp	PeakType	MouseID	2.99	275.18	0.000
	Peak: binary	lmer	BodyTemp	PeakType	MouseID	567891.15	-36.35	0.000